Thesis-1985D-C257l

Dissertation

Caraballo, Nemesio, 1950-

Page Number 109

- ☐ Images
- ☐ Foldouts
- ☐ Maps

- ☐ Scanned
- ☐ Clean-up
- ☐ PDF

☐ Archive MSF ☐ Projects

VS Verified

8/26 Date

LASER LIGHT SCATTERING STUDY OF LOCAL ORDER IN SHEARED COLLOIDAL LIQUIDS

By

NEMESIO CARABALLO

Bachelor of Science in Education
Catholic University of Puerto Rico
Ponce, Puerto Rico
1971

Master of Science
University of Arkansas
Fayetteville, Arkansas
1981

Submitted to the Faculty of the
Graduate College of the
Oklahoma State University
in partial fulfillment of
the requirements for
the Degree of
DOCTOR OF PHILOSOPHY
December, 1985

LASER LIGHT SCATTERING STUDY OF LOCAL ORDER IN SHEARED COLLOIDAL LIQUIDS

Thesis Approved:

Bruce J Ackerson
Thesis Adviser

Virgil L Scott

Richard C. Powell

M G Rockley

Norman N. Durham
Dean of the Graduate College

TO MY FATHER

ACKNOWLEDGMENTS

The author wishes to express sincere appreciation to his major adviser, Dr. Bruce J. Ackerson, for his assistance and guidance throughout the course of this work and also for initiating me into the field of Digital Image Processing. Appreciation is also extended to the other members of the committee, Dr. H. L. Scott, Dr. R. Powell and Dr. M. G. Rockley. Additional thanks are also extended to Dr. G. P. Summers and Dr. H. O. Spivey for serving as members in my original committee.

Also gratitude is extended to Aslam Chowdhury for his friendship and also for giving his time to help me taking the pictures.

We gratefully acknowledge the support by the National Science Foundation, Division of Material Research, Low Temperature Physics Grant Nos. DMR 81-16119 and DMR 85-00704, and the University Center for Water Research.

Finally, the author expresses gratitude to his wife, Maria, for her understanding and encouragement and for the typing of the manuscript.

TABLE OF CONTENTS

Chapter Page

TABLE

LIST OF FIGURES

Figure Page

CHAPTER I

INTRODUCTION

A. Statement of the Problem

It has been known for many years that due to Coulombic interactions, charged particles in an aqueous environment can exhibit interparticle ordering over distances considerably greater than the particle diameter. For sufficiently strong interactions (low ionic strength or high charge), solid-like structures (1) can be formed where each particle is constrained by interparticle forces to a particular lattice site. With weaker interactions (increased ionic strength or decreased charge) the long-range order is destroyed, but considerable short-range order can persist giving a liquid-like structure (2). Recently, there have been a number of studies concerning the properties of dilute colloidal suspensions. The similarity of these colloid systems to molecular fluids has proved remarkable and made them ideal candidates to test many theories of condensed phases, under both equilibrium and nonequilibrium conditions (3).

Because the particle separations are large in the colloidal suspensions of interest, laser light scattering can be used to determine collective structure, much like x-ray diffraction is used in analyzing collective atomic structure.

Figure (1-a) shows a typical scattering pattern from a very dilute colloidal system of strong interacting particles called a "colloidal liquid". The bright intensity ring concentric with the incident beam (in the center of the picture) is referred to as the first Debye-Scherrer ring and is typical of scattering from fluid-like or amorphous phases. It is not sharp as in a solid powder pattern and its dimension in k-space gives a measure of the average particle separation. The five bright dots shown in figure (1-a) are fixed reference points.

For small particles (4) the scattered light intensity $I(\bar{k})$ is proportional to the structure factor $S(\bar{k})$, where $S(\bar{k})$ is related to the pair correlation function $g(\bar{r})$ (sometimes called radial distribution function) by a Fourier transform.

$$S(\bar{k}) = 1 + (1/n)\int \left[g(\bar{r}) - 1\right] \exp(i\bar{k}.\bar{r})\, d\bar{r} \qquad (1\text{-}1)$$

Here n is the colloidal particle concentration and $\bar{k}$ is the scattered wave vector. The pair correlation function $g(\bar{r})$ is a measure of the probability of finding a particle at position $\bar{r}$ given another particle at the origin.

We are concerned here with fluid systems undergoing a steady linear shear flow, at shear rate w. Figure (1-b) shows a typical scattering pattern from a colloidal liquid undergoing shear flow; the five bright dots are fixed reference points illustrating the position of the ring when no shear is applied. As far as we know no similar direct measurement of the shear induced distortion of the local

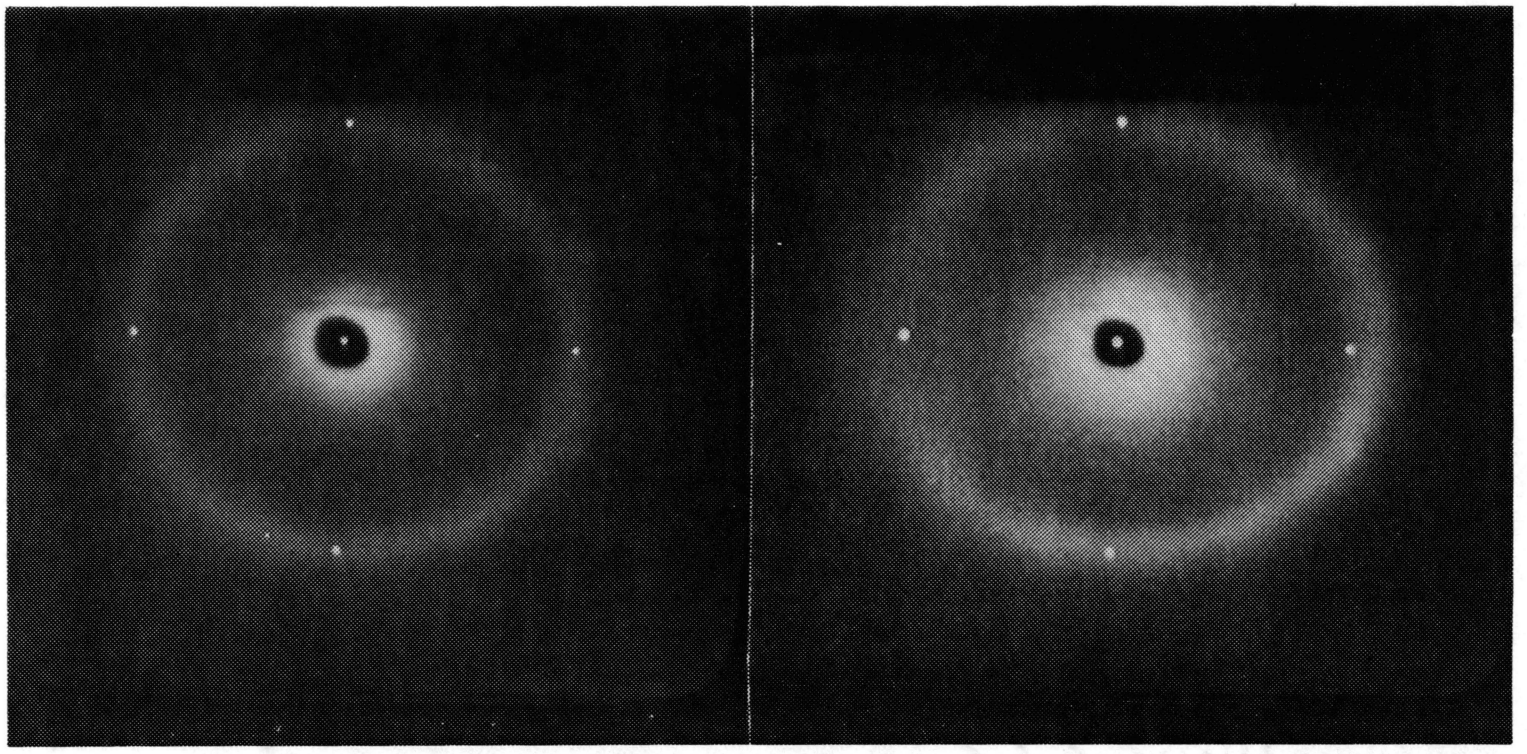

Figure 1. Observed Scattering Pattern of Dilute Colloidal Liquids When the Shear Cell is in the Configuration 1 Described in Page (32) and at -45° with Respect to the Incident Beam (a) Sample in Equilibrium (b) Sample Undergoing Shear

fluid particle order has been made for pure fluids. The reason for that is that the shear rate must compete with molecular relaxation times τ to give an observable effect (the distortion can be characterized by the dimensionless group τw). Thus for a pure fluid where $\tau = 10^{-12}$ sec , shear rates of $\sim 10^{11}$ sec^{-1} are required. Since such experiments are not easily performed, computer simulation experiments of atomic systems have been conducted to study both the shear induced distortion of the pair correlation function $g(\bar{r})$ and the shear viscosity for pure fluids.

On the other hand relaxation times are much slower in colloidal systems ($\tau = 10^{-2}$ sec) such that modest rates of shear can produce significant effects. An inspection of the scattering pattern of colloidal liquids undergoing shear flow shows the following:

1. Under equilibrium conditions (no shear applied) the scattering pattern is spherically symmetric but becomes ellipsoidal when a shear is applied. This shear induced distortion can be observed in figure (1-b).

2. For small rates of shear, the major axis of the ellipsoid is approximately at 45° with respect to the direction of the velocity in the velocity shear plane.

3. When a shear is applied the intensity distribution on the ring (called Debye-Scherrer ring) is not constant but becomes angular dependent.

Although some theories have been developed in an effort to explain the scattering pattern of dilute colloidal

systems undergoing shear flow; there is very little experimental data to support these theories. As far as we know the only experimental evidence reported concerning the shear induced distortion of the scattering pattern comes from the work of Ackerson and Clark (2), and very little numerical data was reported.

B. Purpose of This Thesis

1. To measure the structure factor of liquid-like colloidal suspensions under equilibrium and nonequilibrium conditions.

2. To quantify the dependence of the scattered intensity on the rate of shear.

3. To quantify the dependence of the distortion of the scattering pattern on the rate of shear.

4. To compare the experimental results with those predicted by the theories in this field.

This information can be used to determine the effect of the rate of shear in the microscopic structure of these colloidal systems. Perhaps this information can be even extrapolated to predict how a atomic system will behave in similar conditions.

In Chapter II we present a literature review. It begins with a review of previous experimental work in colloidal systems under a variety of conditions. In particular we review shear viscosity measurements and the effect of the shear flow on the microscopic structure of the colloidal

systems. Following the experimental work we review some of the computer simulations for pure fluids which demonstrate analogous behavior. We conclude Chapter II with a review of the theoretical efforts to describe the structure factor and the pair correlation function of dilute colloidal suspensions undergoing shear flow.

In Chapter III we discuss the experimental details as well as data analysis techniques. We begin the chapter by describing the nature of the colloidal samples, and a description of the shear cell and shear rate calibrations. The experimental set up used for light scattering measurements, details concerning the optical alignment, and the importance of rotating the sheared colloidal sample is also discussed. This is followed by a discussion of the techniques used to process the pictures obtained when the scattering pattern is photographied or recorded on video tape. We conclude that chapter by discussing the way that the data is manipulated and corrected to account for a variety of distortions, including the distortion introduced by the optical system and the refraction distortion introduced by the shear cell. The noise and fluctuations in the intensity introduced by the digitizing process is also considered. Finally other corrections like small gap effects and multiple scattering are discussed.

In Chapter IV we present our experimental results; the interpretation of the experimental data and its correspondence to the theory is discussed through the

analysis of the nonequilibrium structure factor. Results obtained from two different samples are presented and analyzed. In order to compare the experimental results with the theory, the nonequilibrium structure factor is evaluated numerically. Two different equilibrium structure factors $S(k,0)$ are used in the calculations; the first one is based on a one dimensional harmonic coupled chain of colloids (5), the second one is based on the hypernetted chain approximation (6).

The last chapter, Chapter V, gives a summary of results and suggestions for future work.

CHAPTER II

REVIEW OF LITERATURE

A. Experimental Work on Colloidal Systems

In this section we review some of the experimental work that has been done in colloidal systems; the material presented is organized in such a way that high concentrated systems are discussed first and low concentrated systems are discussed last.

One of the first to analyze microscopic colloidal particle structure was Hoffman (7), who used white light scattering to study highly concentrated suspensions of monosized polyvinyl chloride spheres in dioctyl phthalate undergoing shear flow. These observations provide an explanation for the observed abrupt increase in the viscosity (discontinuous shear thickening) at a certain shear rate. He interprets this effect as a flow instability in which two dimensional hexagonally close packed (hcp) layers of spheres slip past one another at low shear rates (indicated by a star-like scattering pattern), break up into less ordered arrays of spheres (no star pattern) at a critical shear rate. The extra energy required by the spheres when they jam into one another during flow causes the discontinous jump in the viscosity at the instability point. Far above the

discontinuity point ordered flow occurs once again and a decrease in the viscosity is observed (return of the star pattern). A similar effect has been observed by Strivens (8).

Laun (9) has studied the viscous behavior of aqueous dispersions of nearly monodisperse charge stabilized polymers spheres (250 nm in diameter) under a wide range of particle concentrations. His experimental results are shown in figure (2). For small volume fractions the shear viscosity is constant as a function of shear rate indicating a Newtonian behavior. However as the concentration increases, the shear viscosity becomes strongly dependent on the shear stress. At high volume fractions the samples showed a shear thinning effect at low shear stress and a shear thickening effect at intermediate shear stresses; followed by shear thinnig at largest shear stresses. These results are similar to those of Hoffman with the exception that non discontinuous viscosity behavior was observed.

More recently M. Tomita and T. G. M. Van den Ven (10) have studied the microstructure in suspensions of electrically interacting particles at concentrations somewhat lower than those of Hoffman. As the shear rate was increased from zero to intermediate values, the observed scattering pattern comprized of an hexagonal arrangement of spots was observed to become less clear before becoming clear again as the shear rate increased further. Although the lattice order did not completely disappear at any shear rate, a change in the structure was observed. They inferred from measurements

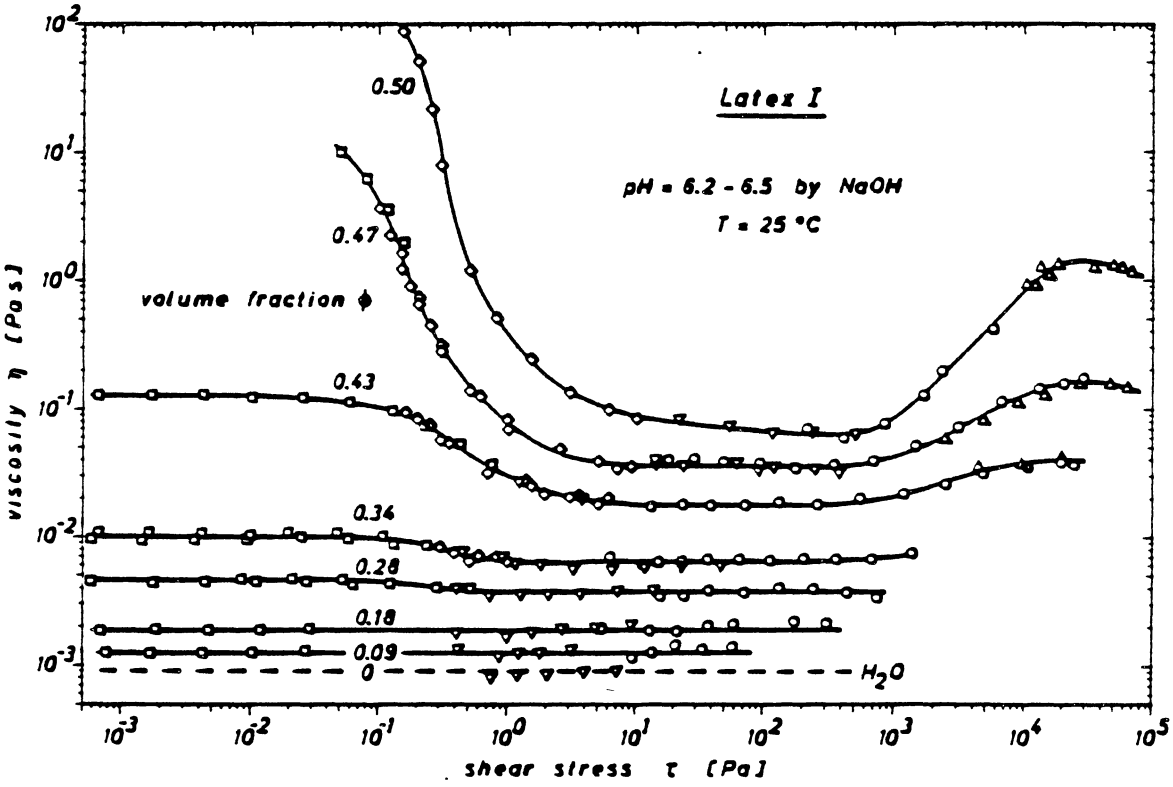

Figure 2. Viscosity Functions at Different Particle Concentrations (from Reference (9))

of the hexagonal scattering pattern that at high shear there was an expansion of the spacing between the parallel layers which occupy planes of constant velocity in the shear flow and a compression of the hexagonal packing in the two dimensional layers. Their samples showed no discontinuity in the viscosity in contrast to Hoffman's samples.

Ackerson and Clark (2) have investigated dilute systems of strongly interacting particles. Their samples were prepared using nearly monodisperse DOW polysterene plastic spheres (concentration of solid of approximately 0.17 wt %). A small amount of ion-exchange resin was used to maintain the sample in a highly deionized state. They have shown that when the colloidal solid is subjected to increasing shear, it will pass through a series of structures before melting and finally exhibiting an amorphous or liquid-like order. The observed transitions from solid to a liquid-like system are as follows: a) a bcc structure is observed at equilibrium (polycrystaline or oriented twin depending on shear history), b) as the shear is increased a distorted bcc structure evolves into a distorted 2D hcp structure, c) for larger shear rates the 2D hcp layers break up into strings of evenly spaced particles aligned parallel to the flow direction. Finally as the shear rate is further increased, a transition to short-range or liquid-like order takes place. This shear induced melting effect also has been observed in more concentrated aqueous suspensions (which are fcc in equilibrium) by Pieranski (11).

For weaker interactions between the colloidal particles a liquid-like structure is observed at rest. A typical scattering pattern is shown in figure (1-a). Brown et al. (12) have used light scattering to study aqueous dispersions of charged polysterene spheres. They have measured the equilibrium structure factor and calculated the radial distribution function by Fourier transformation of the intensity data.

Perhaps, Ackerson and Clark (2) were the first ones to use light scattering to study very dilute colloidal systems of electrically interacting particles undergoing shear flow. They observed that the spherical scattering pattern at equilibrium becomes elliptically distorted when the sample is sheared. The line of maximum distortion is at 45° respect to the flow velocity. Their data showed that for very dilute systems the distortion with respect to the equilibrium value is directly proportional to the applied shear rate w. They explained their results using a theory based on the "Stoke's model" (this theory is discussed later in this chapter).

B. Computer Simulations for Pure Liquids

It has been evident ever since the formulation of statistical mechanics that progress toward a quantitative theory of condensed fluids is limited by mathematical and not conceptual difficulties. The advent of large scale computers has vastly increased the power of numerical techniques and it is therefore natural to ask what additional contribution to

the understanding of dense fluids can be made through the computer.

A widely used computer simulation technique is nonequilibrium molecular dynamics (NEMD). Basically, in this method one uses the computer to solve Newton's equations of motion for a system of N atoms interacting with some assumed intermolecular potential. The use of periodic boundary conditions is necessary, since with available computers N is limited to less than a few thousands.

The pair distribution function of dense fluids undergoing shear was first studied by Ashurst and Hoover (13) using NEMD, they investigated a soft-sphere and a Lennard-Jones system of particles. Their computer simulation supported the "Stoke's model" later used by Ackerson and Clark (2) in interpreting colloidal data.

One of the most surprising and fundamental phenomena revealed by NEMD is that simple pure fluids can exhibit non Newtonian behavior. For example shear dilatancy has been observed (i.e., the hydrostatic pressure is a function of the rate of shear). In order to explain this effect Evans and Hanley (14) hypothesised that the first law of thermodynamics for shearing fluids must be modified as

$$dE = dQ - pdV + \alpha\, dw \qquad (2\text{-}1)$$

where w refers to the shear rate and the function α is calculated using

$$\alpha(T,V,w) = \int_{V}^{\infty} \frac{\partial p(V',T,w)}{\partial w} \, dV' \qquad (2\text{-}2)$$

A result obtained in their work was that a Lennard-Jones fluid showed a shear dependent critical point. It is interesting to note that a shift in the critical point of a binary-component fluid has been observed experimentally using light scattering by Beysens and Gbadamassi (15).

Hess and Hanley (16) have used NEMD to study a 108 particles system interacting with an inverse twelfth potential at a state point close to the melting transition. They have studied the radial distribution function $g(\bar{r})$ for different values of the shear rate. Results from their computer simulations indicate that the system of particles showed a non Newtonian behavior.

Subsequently, Hanley et al. (17) have calculated scattered light intensity plots for the same system of 108 particles subjected to a shear rate. Remarkably they have been able to replicate the essential features of the experimental results discussed in page 4 for colloidal systems, namely that the Debye-Scherrer rings become distorted under shear and that the intensity becomes a function of the polar angle. Furthermore, in their computer simulations, they have observed a rotation of the major axis of the ellipse towards the direction of the velocity gradient; this phenomena is an indication of a non Newtonian behavior.

One of the properties most widely studied using NEMD is the shear viscosity. Several authors, including Ashurst and Hoover (13, 18), Evans (19), EU (20) and Erpenbeck (21), have studied the shear viscosity of a variety of systems using NEMD. Although computer simulations show that for simple fluids the viscosity decreases with increasing shear (i.e., shear thinning), the small shear rate is not well understood. While early NEMD evidence seemed to support a $\{\sinh^{-1}(\tau w)\}/\tau w$ form (18, 20), more recent calculations have been interpreted in favor of $w^{\frac{1}{2}}$ dependence (19) which is qualitatively in agreement with some theoretical predictions (22) as an approximate result in kinetic theory.

$$\eta(w) = \eta(0) - bw^{\frac{1}{2}} \qquad (2\text{-}3)$$

where $\eta(0)$ is the Newtonian (0 shear rate) viscosity, w is the shear rate and b is a constant independent of w.

In his computer simulations Erpenbeck (21) has observed that when a hard sphere system is subjected to a high shear rate, there is a phase transition in which the system undergoes a two dimensional ordering in the plane perpendicular to the flow. Individual particles remain localized within a cylinder parallel to the direction of the flow. This effect is accompanied by a sharp decrease in the viscosity.

Finally, Evans (23) has used NEMD to study the viscosity in a system of 108 soft spheres interacting with an inverse twelfth potential $\Phi(r)$. In his computer simulations he

observed that with the imposition of a steady shear, a crystal melts through a series of intermediate phases similar to that suggested experimentally by Ackerson and Clark.

C. Theory for the Liquid Pair Distribution Distortion with Application to Colloidal Suspensions

As explained earlier, for small particles the scattered light intensity $I(\bar{k})$ is proportional to the structure factor $S(\bar{k})$, where $S(\bar{k})$ is related to the pair correlation function $g(\bar{r})$, by a Fourier transform.

Under equilibrium conditions $g(\bar{r})$ and $S(\bar{k})$ are spherically symmetric; but when the colloidal suspension is sheared the nonequilibrium structure factor $S(\bar{k},w)$ shows a distortion with respect to the equilibrium value $S(k,0)$. Since light scattering gives a direct measurement of $S(\bar{k},w)$ much of the theoretical effort is directed to the calculation of $S(\bar{k},w)$. Recently, several theories have been developed to calculate the nonequilibrium functions $S(\bar{k},w)$ and $g(\bar{r},w)$. Since dilute colloidal systems show strong similarities with real atomic systems the development of the theory is based on a generalized form of the diffusion equation for pure fluids. In this thesis we examine the following theories: a) a theory based on the Stoke's model (2,13), b) the theory of Hess (24) and c) the theory of Ronis (3,6).

Since we are working with liquids undergoing a small shear flow, it will be appropiate to review some basic concepts of fluid mechanics. The interested reader will find

a brief introduction in Appendix A.

1. Stoke's Model

The pair distribution function $g(\bar{r},w)$ is found under the assumption that it is solution of the Smoluchowski (25) equation

$$\frac{\partial g(\bar{r})}{\partial t} = \frac{2k_bT}{\zeta}\ \bar{\nabla}\cdot\left[\bar{\nabla}g(\bar{r}) + \frac{g(\bar{r})}{k_bT}\ \bar{\nabla}\Phi(r)\right] - \bar{r}\cdot\bar{\nabla}\ \bar{V}\cdot\bar{\nabla}\ g(\bar{r}) \qquad (2\text{-}4)$$

The term k_bT/ζ is interpreted as the diffusion coefficient (i.e., $Ds = k_bT/\zeta$). The first term in the right hand side gives the free diffusion contribution, the second term gives the effect due to particle interactions and the last term gives the contribution due to the shear.

For the remainder of this section, it is assumed that the system is incompressible (i.e., $\bar{\nabla}.\bar{V} = 0$) and that it is undergoing linear shear flow, with $\bar{V} = wx\hat{y}$, where w is the shear rate.

When a small shear is applied the equilibrium distribution function $g(r,0)$ will be slightly distorted, consequently, equation (2-4) is solved using a perturbation method. In this case we write (26, 27)

$$g(\bar{r},w) = g(r,0)\left[\ 1 + W(\bar{r},w)\ \right] \qquad (2\text{-}5)$$

where the small perturbation $W(\bar{r},w)$ is to be determined using equation (2-4); the equilibrium value $g(r,0)$ is given by

$$g(r,0) = \exp\left[-\Phi(r)/k_bT\ \right] \qquad (2\text{-}6)$$

where $\Phi(r)$ is the potential of mean force. Using equation (2-4), (2-5) and (2-6) we obtain the following differential equation

$$\nabla^2 W(\bar{r}) - \frac{1}{k_b T}\,\Phi'(r)\,\frac{\partial W}{\partial r} = \frac{-\zeta w}{2(k_b T)^2}\,\Phi'(r)\, r \sin^2(\theta)\sin(\phi)\cos(\phi) \qquad (2\text{-}7)$$

In writing equation (2-7) we have neglected a second order term in proportional to $\nabla W(\bar{r},w)$. We have also assumed that $g(\bar{r},w)$ is time independent.

For details concerning boundary conditions the reader is referred to Croxton (26) and Cole (27). To solve equation (2-7) it is assumed that $W(\bar{r},w)$ has the same angular dependence as the right hand side of equation (2-7)

$$W(\bar{r},w) = \frac{\zeta}{2k_b T}\, w\, u(r)\, \sin^2(\theta)\sin(\phi)\cos(\phi) \qquad (2\text{-}8)$$

where the unknown function $u(r)$ is a function of r only. Using equation (2-5) and (2-8) we obtain

$$g(\bar{r},w) = g(r,0)\left[1+ \frac{\zeta}{2k_b T}\, wu(r)xy/r^2\right] \qquad (2\text{-}9)$$

Note that the term xy/r^2 can be written as a linear combination of spherical harmonics

$$xy/r^2 \sim Y_2^2 - Y_2^{-2} \qquad (2\text{-}10)$$

By direct substitution of equation (2-9) in equation (A-6) we obtain the following expression for the potential part of the stress tensor

$$\overleftrightarrow{\sigma_\phi} = (n^2/2)\int \hat{r}\,\hat{r}\,\Phi'(r)\, g(r,0)\left[1 + \frac{\zeta w}{2k_b T}\,\frac{xy}{r^2}\, u(r)\right] r\, d\bar{r} \qquad (2\text{-}11)$$

After an integration over the angles the following result is obtained

$$\overleftrightarrow{\sigma}_{\phi} = \frac{2}{3}\pi n^2 \left(\hat{x}\,\hat{x} + \hat{y}\,\hat{y} + \hat{z}\,\hat{z}\right) \int \Phi'(r)\, g(r,0)\, r^3\, dr$$

$$+ \frac{\zeta n^2 \pi w}{15 k_b T} \left(\hat{x}\,\hat{y} + \hat{y}\,\hat{x}\right) \int \Phi'(r)\, g(r,0)\, u(r)\, r^3\, dr \qquad (2\text{-}12)$$

In fluids and dense gases, the kinetic part of the stress tensor is negligible (approximately 10% contribution); consequently, equation (2-12) represents the dominant part of the stress tensor. Using the macroscopic definition of the stress tensor (see Appendix A equation (A-3)) and equation (2-12) we obtain the following expressions for the pressure and the viscosity

$$p_{\phi} = -(2\pi n^2/3) \int \Phi'(r)\, g(r,0)\, r^3\, dr \qquad (2\text{-}13)$$

$$\eta_{\phi} = \frac{\zeta \pi n^2}{15 k_b T} \int \Phi'(r)\, g(r,0)\, u(r)\, r^3\, dr \qquad (2\text{-}14)$$

Having derived equation (2-14) there is still the task of determining the unknown function u(r). In the Stoke's model (Ashurst and Hoover, 1975) the viscous stress of a fluid arising from the interaction of the particles ηw, is approximated by the elastic stress of a solid γG, where the strain γ is equivalent to the rate of strain times a phenomenological relaxation time τ. In this model τ is given by

$$\tau = \eta/G \tag{2-15}$$

An expression for the shear modules G has been derived by Fisher (28)

$$G = \frac{2\pi n^2}{15} \int \frac{d\left[r^4\ \Phi'(r)\right]}{dr}\ g(r,0)\ dr \tag{2-16}$$

Integrating the last equation by parts and using equation (2-15), the following expression is obtained for the viscosity

$$\eta = \frac{-2\pi\tau n^2}{15} \int \Phi'(r)\ \frac{dg(r,0)}{d\ln(r)}\ r^3\ dr \tag{2-17}$$

Comparing equation (2-17) with equation (2-14) we find that u(r) is given by

$$u(r) = \frac{-2k_b T\tau}{\zeta}\ \frac{d\ln g(r,0)}{d\ln(r)} \tag{2-18}$$

Once the function u(r) is obtained we use equation (2-9) to obtain the final form for the function $g(\bar{r},w)$

$$g(\bar{r},w) = g(r,0) - \tau w(xy/r)\ \frac{dg(r,0)}{dr} \tag{2-19}$$

The last equation is valid for small shear rates w. In this case we see that the following equation is equivalent when expanded to first order in a Taylor series expansion (i.e., expanding equation (2-20) in Taylor series we obtain equation (2-19)).

$$g(\bar{r},w) = g(r - \tau wxy/r) \tag{2-20}$$

The nonequilibrium structure factor $S(\bar{k},w)$ is obtained by a

Fourier transform of the last equation. The result is (2)

$$S(\bar{k},w) = S(k - \tau w \frac{k_x k_y}{k}) \tag{2-21}$$

By means of a Taylor expansion the last equation can be written as

$$S(\bar{k},w) = S(k,0) - \tau w \frac{k_x k_y}{k} \frac{dS(k,0)}{dk} \tag{2-22}$$

where $S(k,0)$ represents the equilibrium structure factor. Equation (2-21) was used by Ackerson and Clark (2) to explain their colloidal data.

2. The Theory of Hess

The point of departure in Hess' theory (24) is also the same Smoluchowski equation for the pair correlation function $g(\bar{r})$ (see equation (2-4)) written in the following form:

$$\frac{\partial g(\bar{r})}{\partial t} = \frac{1}{\tau} \frac{\partial}{\partial R_\mu} \left[\frac{\partial g(\bar{r})}{\partial R_\mu} - \frac{g(\bar{r})}{g(r,0)} \frac{\partial g(r,0)}{\partial R_\mu} \right] - \omega_\mu L_\mu g(\bar{r}) - \gamma_{\mu\nu} \frac{\partial R_\nu g(r)}{\partial R_\mu} \tag{2-23}$$

Here τ is a relaxation time coefficient. In writing the last equation, the velocity gradient tensor appearing in equation (2-4) has been decomposed into a symmetric part $\gamma_{\mu\nu}$ and an antisymmetric part involving ω_μ.

$$\omega_\mu \equiv \tfrac{1}{2}(\bar{\nabla} \times \bar{V})_\mu \tag{2-24}$$

$$\gamma_{\mu\nu} \equiv \tfrac{1}{2}(\nabla_\mu V_\nu + \nabla_\nu V_\mu) \tag{2-25}$$

$$\bar{R} \equiv \bar{r}(\tau D_s)^{-\frac{1}{2}} \tag{2-26}$$

$$\bar{L} \equiv \bar{R} \times \frac{\partial}{\partial \bar{R}} \qquad (2\text{-}27)$$

Consequently, the last two terms in equation (2-23) describe the change of $g(\bar{r},w)$ due to the presence of a shear flow. The first term in the right hand side of equation (2-23) corresponds to the free diffusion, the second term gives the approximation for the effect due to particle interactions.

To obtain $g(\bar{r})$ from equation (2-23) Hess starts with a method similar to the one used in the Stoke's model (see equations (2-5) and (2-6)). To determine the small perturbation term $W(\bar{r})$, he chooses a complete set of orthonormal functions Φ_J and writes:

$$W(\bar{r}) \equiv \Sigma\, a^J \Phi_J \qquad (2\text{-}28)$$

The problem is reduced to the calculation of the expansion coefficients a^J using equation (2-23) and the orthogonality properties of Φ_J.

In particular, he discusses the results for small angle scattering, where the incident beam is normal to the plane determined by $\bar{V}$ and its gradient. For the case where the velocity is parallel to the x axis and its gradient parallel to the y axis, i.e., $\bar{V} = wy\hat{x}$, he obtained the following equation for the nonequilibrium structure factor (assuming a small shear rate w)

$$S(\bar{k},w) = S(k,0) + \tau\, wk \sin 2(\phi - \chi) \frac{\partial S(k,0)}{\partial k} \qquad (2\text{-}29)$$

The last equation includes terms nonlinear in the shear rate. Note that this expression is very similar to the expression obtained using the Stoke's model (equation (23)). The major difference is the term $\sin 2(\phi - \chi)$; ϕ is a polar angle of the vector $\bar{k}$. The angle χ is a measure of the rotation of the scattering pattern, which represents an improvement of the Stoke's model results. The angle χ can be calculated using the expression

$$\chi = \tfrac{1}{2} \mathrm{Tan}^{-1} (\tau w) \qquad (2\text{-}30)$$

3. The Theory of Ronis

The point of departure in Ronis theory (3,6) is a fluctuating diffusion equation model, where a random diffusion current, $F(\bar{k},\omega)$ is added to account for fast, short wavelength processes not adequately described by the macroscopic theory.

$$(i\omega + k^2 D_k)\, N(\bar{k},\omega) = w k_y \frac{\partial N(\bar{k},\omega)}{\partial k_x} + i\bar{k}\cdot\bar{F}(\bar{k},\omega) \qquad (2\text{-}31)$$

In the last equation $N(\bar{k},\omega)$ is the Fourier transform of the colloid particle density; D_k is a $\bar{k}$ dependent diffusion constant which approximates the colloidal particles direct interaction. Note that this equation (approximately) corresponds to a Fourier transform (in time and space) of a Langevin form for equation (2-4). It is assumed that the shear velocity is $\bar{V}(r) = wx\hat{y}$ and that the random diffusion current has a correlation given by:

$$\langle F(\bar{k},\omega).\, F^{\dagger}(\bar{k}',\omega')\rangle \equiv 2(2\pi)^4 n\delta(\bar{k}-\bar{k}')\delta(\omega-\omega')\; D_k\; S(k,0) \qquad (2\text{-}32)$$

The nonequilibrium structure factor $S(\bar{k},w)$ is obtained from the following relation

$$S(\bar{k},w) = (1/n)\ \langle N(\bar{k})\ N(-\bar{k})\rangle \qquad (2\text{-}33)$$

This is found by solving equation (2-31) for $N(\bar{k},\omega)$ using the integrating factor

$$\exp\int\left[\frac{-i\omega}{wk_y} - \frac{k^2 D_k}{wk_y}\right]\, dk_x \qquad (2\text{-}34)$$

Then the problem consist in calculating $S(\bar{k},w)$ using equation (2-32) and (2-33). The result is (6)

$$S(\bar{k},w) = \frac{2Ds}{|k_y w|}\int_L^{\infty} d\tilde{k}_x(\tilde{k}_x^2 + k_y^2 + K_z^2)\ \exp(-A)$$

$$A \equiv \frac{2Ds}{|k_y w|}\int_L^{\tilde{k}_x} dx\ \frac{(x^2 + k_y^2 + k_z^2)}{S(x,0)} \qquad L \equiv \frac{k_x k_y w}{|k_y w|} \qquad (2\text{-}35)$$

Assuming the starting equation is correct, this result is valid for all shear rates and $\bar{k}$ values and can be evaluated using equilibrium experimental data for $S(k,0)$ or results from model calculations.

CHAPTER III

EXPERIMENTAL DETAILS AND DATA ANALYSIS TECHNIQUES

A. Experimental Details

1. Colloidal Samples

The samples used are nearly monodisperse (standard deviation of approximately 3 nm) DOW polysterene plastic spheres suspended in deionized, distilled water. Two different samples were analyzed during this research.

Sample A: This sample consist of spheres, 220 nm in diameter, suspended in water. The volume fraction of solids is .0017.

Sample B: In this sample the diameter of the spheres is 198 nm. The volume fraction of solids is also .0017.

A small amount of H-OH ion exchange resin was added to the samples to maintain them in a highly deionized state. The observed scattering pattern of sample A indicated a mixed "solid" and "liquid" coexistence, while sample B indicated a weaker structure being in a pure "fluid" state in equilibrium.

2. Experimental Set Up

Figure (3) shows a top view of the experimental set up used to measure the scattering pattern of colloidal liquids undergoing shear flow.

An argon ion laser operating at a wavelength of 488 nm was used to illuminate the sample. The shear cell B (containing the colloidal sample) was immersed in a water tank A. This was done to match the refractive index of the sample and the water (the refractive indexes are approximately the same). The shear cell can be rotated about the point F; in this way the angle I can be changed from -60° to $+60^{\circ}$. An electric motor connected to the shear cell by a belt is not shown. The scattered light is projected onto the screen C. The resulting scattering pattern is captured using a video camera D and recorded using a video cassette recorder E. Two different video cameras were used during this research; sample A and sample B (see page 25) were photographied using a Sony video camera model AVC 3250 and a Koyo video camera model TVC-6200-2, respectively. The same lens (Sony zoom lens) was used with both cameras.

3. Shear Cell

Figure (4) is a schematic diagram of the shear cell. A and B are stationary quartz disks of approximately 20.3 cm in diameter and .64 cm in thickness. C is a rotatory quartz disk of approximately 15 cm in diameter and .32 cm in thickness and D is a small piece of glass (glued to disk A)

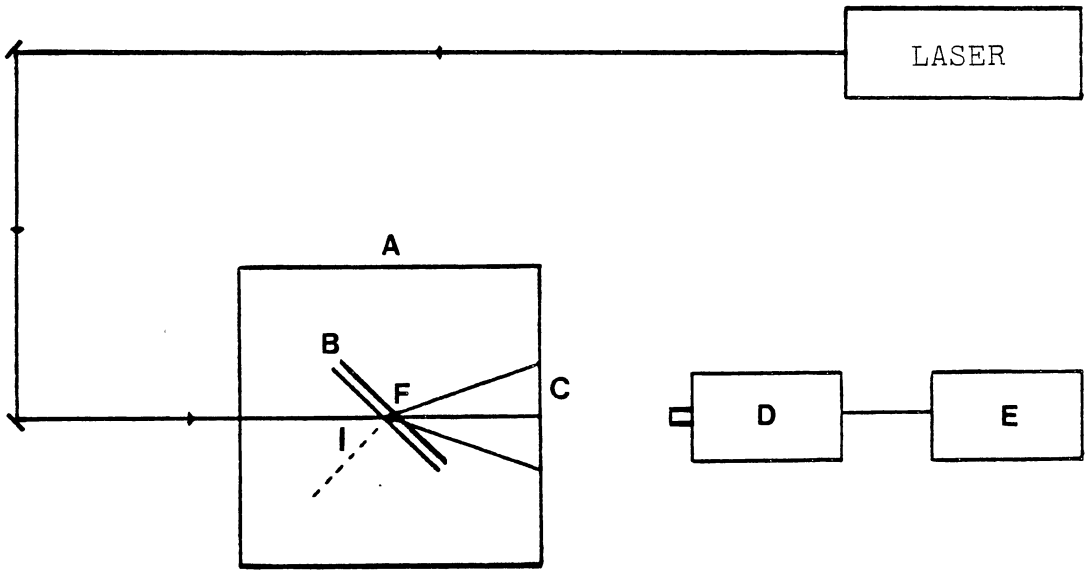

Figure 3. Experimental Set Up to Measure the Scattering Pattern of Colloidal Liquids Undergoing Shear (A) Water Tank (B) Shear Cell (C) Screen (D) Video Camera (E) Videotape Recorder

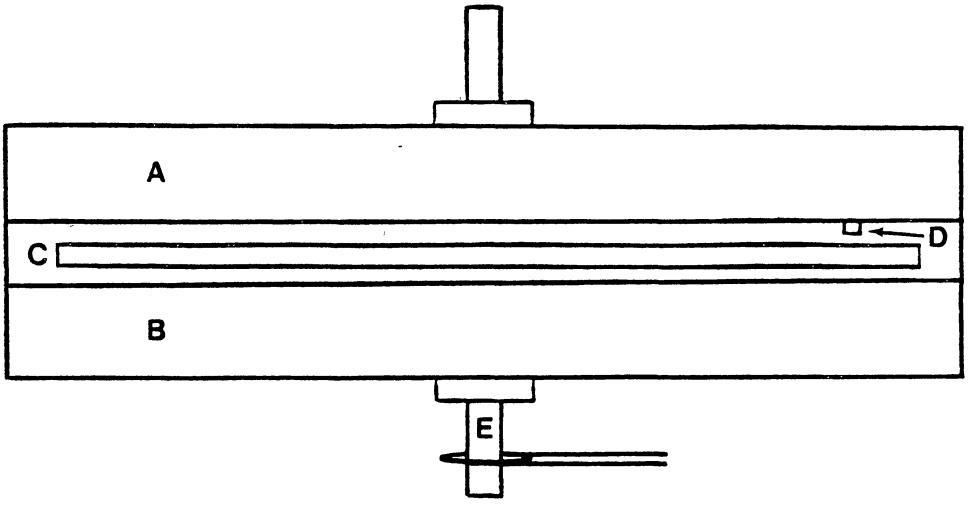

Figure 4. The Shear Cell. The Laser Beam is Focused in the Small Gap Between B and C

of approximately 2 cm in diameter and 1 mm in thickness. The gap in between B and C is approximately 1 mm. The shaft E is directly connected to disk C. The total sample volume is 60 cc. The cell was sealed using a silicon rubber O-ring between disks A and B, and thick teflon quad rings between the shaft and the stationary disks. This seal was air tight and the cell sufficiently clean that highly deionized states are obtainable.

For laser light scattering the laser beam is directed towards the small piece of glass D and focused in the sample contained between C and B. The small volume where the laser is focused is called the scattering volume.

4. Shear Rate Calibration

Figure (5) shows the velocity profile inside the shear cell for the case where the velocity is $\bar{V}=wx\hat{y}$. In this case the shear rate w is defined as follows:

$$w = dV(x)/dx \qquad (3\text{-}1)$$

At the point $x=x_o$ (x_o is the gap spacing between B and C) the velocity of the fluid is the same as the velocity of the rotatory quartz disk C (assuming no slipping between the fluid and the quartz disk), which can be calculated using the following equation:

$$V = 2\pi d_o/T \qquad (3\text{-}2)$$

where d_o is the distance from the scattering volume to the

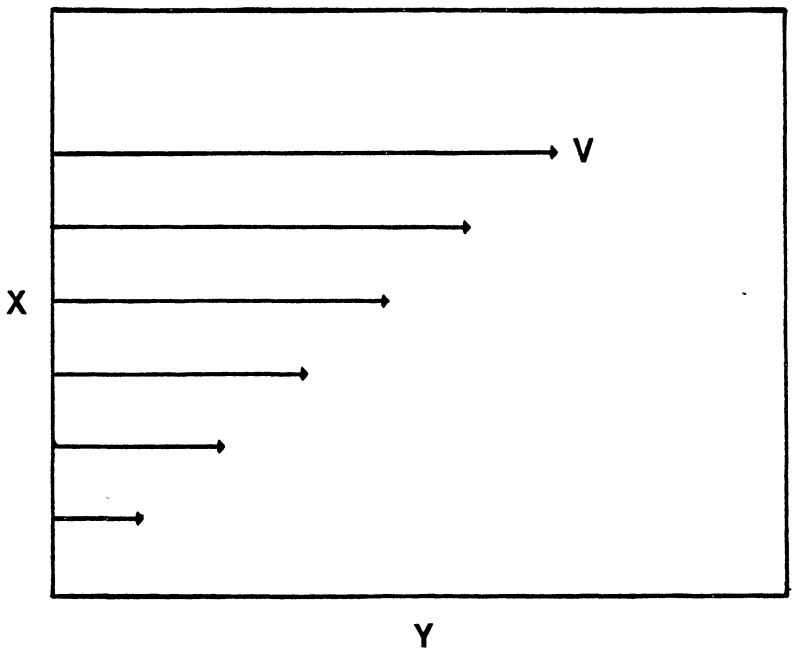

Figure 5. Velocity Profile in the Shear Cell. The Velocity is in the Y Direction and the Velocity Gradient in the X Direction

axis of rotation of disk C; T is the time that disk C takes to complete one revolution and can be measured using a stopwatch. For a 1mm gap and d_o = 6.8 cm we obtain

$$w = 136\ \pi/T \qquad (3\text{-}3)$$

The time per revolution T was measured using a stopwatch and equation (3-3) was used to calculate the shear rate.

5. Optical Alignment and Rotation of the Sample

The initial alignment is performed with no shear applied and the shear cell at 90° ($I=0^{\circ}$) with respect to the incident beam (the laser beam is weakly focused in the small gap between C and B). The design of the shear cell allows us to rotate the cell with the axis of rotation perpendicular to the incident beam and passing through the scattering volume. The purpose of rotating the cell about this point is to examine the effect of the shear flow on the 3-D arrangement of the colloidal particles. With no shear applied the scattering pattern is spherically symmetric and the projection on the screen results in a circular ring (called Debye-Scherrer ring). When the sample is sheared, the scattering pattern is distorted indicating that the 3-D arrangement of particles have also been distorted with respect to the equilibrium configuration.

Our experiment showed that the observed scattering pattern at equilibrium becomes a distorted ellipsoid when the colloidal liquid is sheared. The major axis of this

ellipsoid is in the plane determined by the flow velocity and the velocity gradient and it is approximately at 45^{o} with respect to both axes. Consequently, by rotating the sample, the 3-D arrangement of the particles can be analyzed by examining the 2-D projection of the ellipsoid on the screen.

In order to have a complete view of the 3-D structure of the colloidal sample, two different configurations were analyzed.

a. Configuration 1

This configuration is illustrated in figure (6-a). In this figure the incident beam is in the x direction ($\bar{k}_o = k_o \hat{x}$), the velocity is in the y direction ($\bar{V}=wx\hat{y}$) with a constant velocity gradient in the x direction. The scattering volume is located at the origin and the screen is in the z-y plane. Figure (6-a) also shows the projection of the ellipsoid in the x-y plane. The shear cell design allows us to rotate the cell about the z axis in figure (6-a) or about the y axis in figure (6-b); a rotation of -45^{o} around the z axis in figure (6-a) will project the major axis of the ellipsoid on the viewing screen. Consequently, the observed distortion on the screen will be maximum when the shear cell is at -45^{o} with respect to the incident beam.

b. Configuration 2

This configuration is illustrated in figure (6-b). Note that this geometry is obtained by a rotation of figure

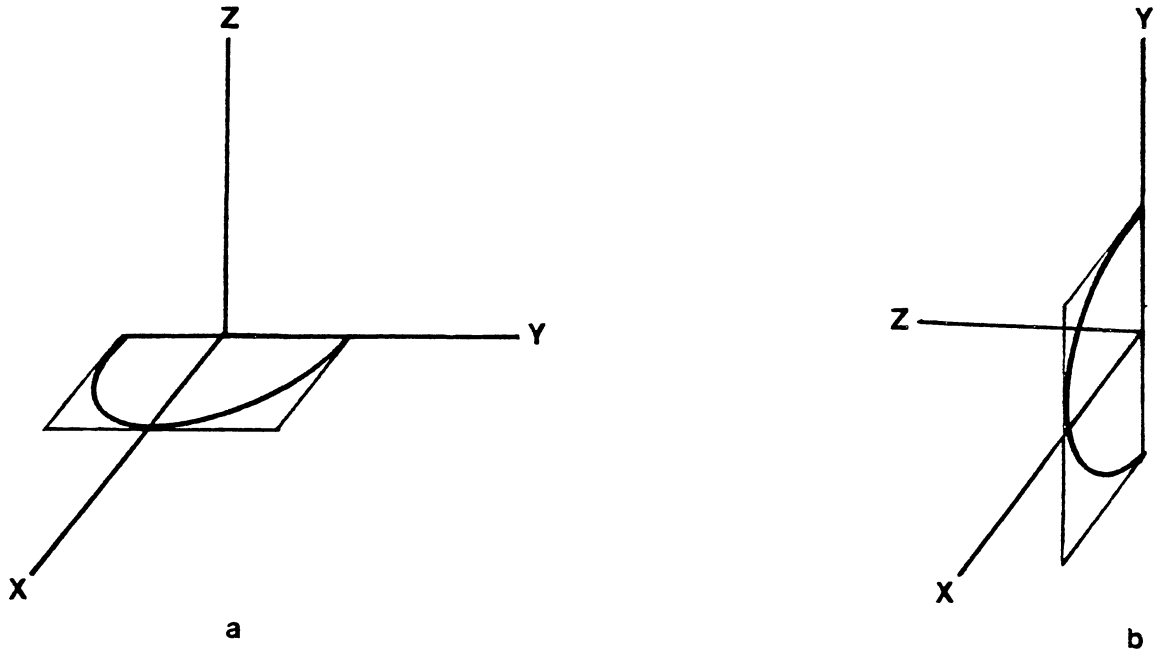

Figure 6. Basis Indicating the two Different Orientations of the Shear Cell (a) Configuration 1 (b) Configuration 2 In Both Cases the Flow Velocity is in the Y Direction, the Velocity Gradient is in the X Direction. The Plane Containing the Major and Minor Axis of the Ellipsoid is Shown

(6-a) by 90° about the x axis. The main difference in this geometry is that now the cell is rotated along the y axis, consequently a 90° rotation about this axis is necessary to project the major axis of the ellipsoid on the screen (located in the z-y plane). The design of the shear cell allows a maximum rotation of 60° , consequently the observed distortion on the screen for this configuration is expected to be less than the previous geometry.

A new basis $\hat{R}1$, $\hat{R}2$ and $\hat{R}3$ can be defined based on the major and minor axis of the ellipsoid. Here r1, r2 and r3 are the dimensions of the observed Debye-Scherrer ring along $\hat{R}1$, $\hat{R}2$ and $\hat{R}3$, respectively. As we will see later, this basis corresponds to the eigenvectors of the stress tensor, the directions of maximun and minimum shear stress. $\hat{R}1$ and $\hat{R}2$ are unit vectors along the lines of maximum and minimum distortion, $\hat{R}3$ is a unit vector along the z direction. This set of axes is shown in figure (7-a), figure (7-b) shows a cross section of the ellipsoid in the R1-R3 plane, and figure (7-c) shows a cross section in the R2-R3 plane.

It must be remembered that theoretically the observed scattering pattern (ellipsoid) can be Fourier transformed to obtain the particle distribution in real space. In practice, however, this involves an enormous amount of data manipulation and computer time (each single picture contains 256 kilobytes of data). Also accurate intensity data is needed to perform a Fourier transform. Nevertheless, since the scattering pattern is highly symmetric, some

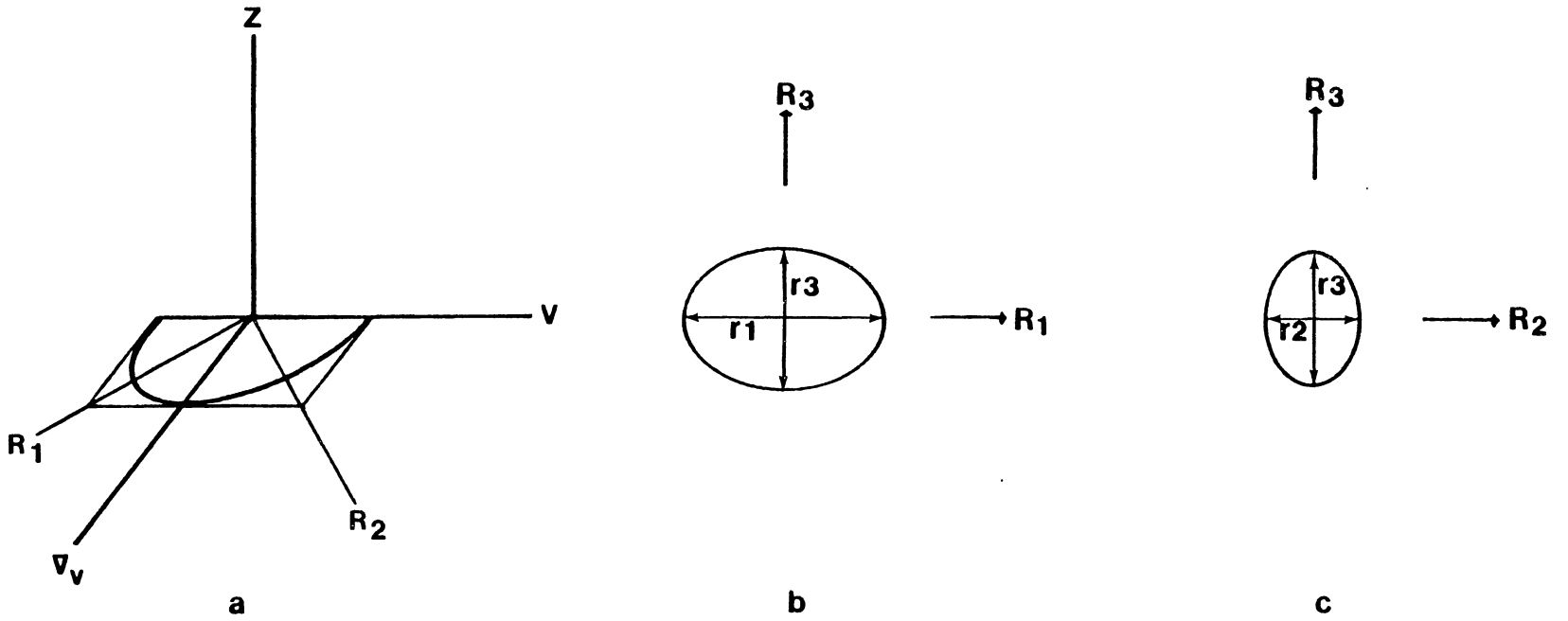

Figure 7. Set of Axes Based on the Direction of Maximum and Minimum Shear Stress. (a) Orientation of This Basis with Respect to the Flow and Velocity Gradient (b) Cross Section of the Ellipsoid in the R1-R3 Plane (c) Cross Section of the Ellipsoid in the R2-R3 Plane

understanding of the shear induced distortion can be obtained by looking at the dimensions of the major and minor axis of the ellipsoid as a function of the shear rate.

6. Image Processing

All the experimental information is recorded on video tape for further analysis. Figure (8) shows a block diagram of the system used for image processing. An Imaging Technology video digitizer interfaced with a LSI-11 computer was used for image processing. The video output of the VCR is sent to the video digitizer, where individual frames in the video tape are digitized; the resulting image is displayed in a video monitor. The digitizing process consist of transforming an individual picture into a two dimensional array of numbers with dimensions of 512 X 480. Each individual point in the array is called a picture element or pixel and can have an intensity value between 0 and 255. The resulting digital image is deposited within a 256 kilobyte video RAM where it is accesible by the LSI-11 computer. In this way the stored image can be manipulated with the computer to perform among others the following operations:

a. Enhance the picture by histogram equalization, gradient operation, filtering, etc.

b. Extract useful information like edges and contour lines

c. Average several pictures for noise reduction

d. Subtract two pictures to detect the deformation of

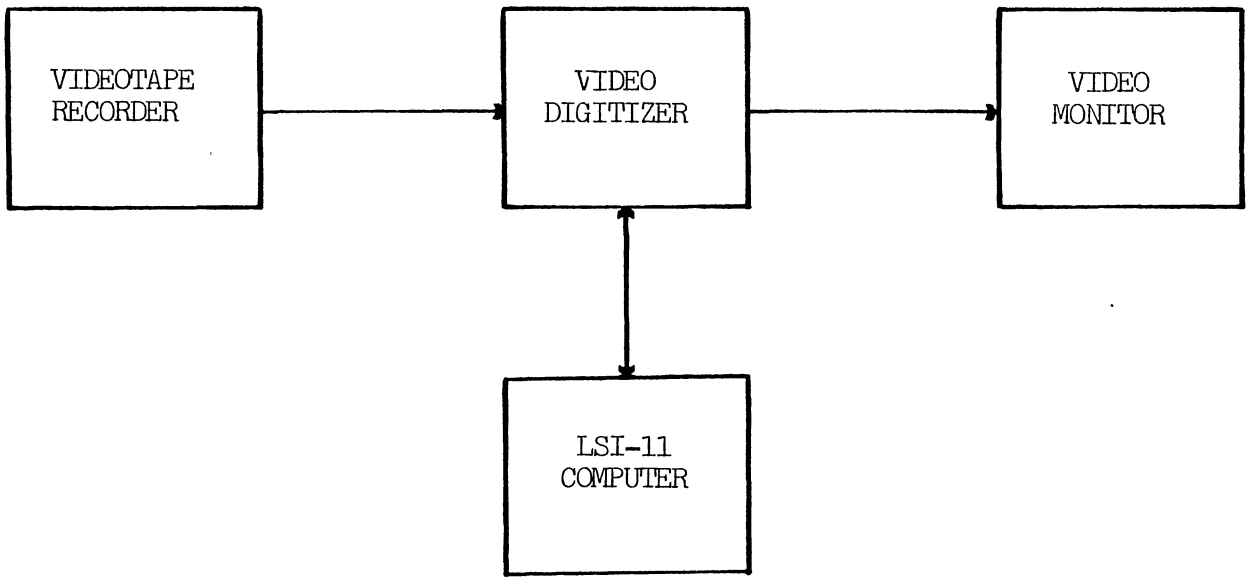

Figure 8. Block Diagram Showing the Arrangement of Apparatus for Digital Image Processing

the scattering pattern

In particular the last two of these operations were used during data adquisition and processing.

It was observed that the digitization process introduces a considerable amount of noise or fluctuations on the value of the intensity; this effect is easily appreciated by scanning the intensity along any particular direction. However, this noise or fluctuations in the intensity can be reduced considerable by taking an average of several pictures. The data reported in this thesis are actually average values where as many as 20 readings were used to calculate the averages.

B. Data Analysis Techniques

Shearing the colloidal sample not only produces radial distortion of the scattering pattern but also affects the angular intensity distribution. To obtain an accurate measurement of this distortion, all the data must be corrected to account for the optical distortion introduced by the video camera and by refractive effects introduced by the quartz disks in the shear cell. These distortion effects, as well as multiple scattering and small gap effects, are discussed next.

1. Optical Distortion of the Video Camera

To estimate optical distortion of the video camera, a polar graph paper was photographied. The resulting picture

was analyzed using the video system, where the diameter of each of four rings was measured along two perpendicular directions. The average diameter, calculated from five different runs are shown in table I.

It can be observed that the distortion (d1/d2) increases as the ring size increases (i.e., as we approach the edges of the picture). All the scattering patterns analyzed (both samples in equilibrium and undergoing shear flow) have approximately the same dimensions as ring #3; consequently, all experimental data presented here include a 1.3% correction factor.

TABLE I

DISTORTION OF THE OPTICAL SYSTEM

	d1(pixels)	d2(pixels)	d1/d2
ring #1	87.0	86.8	1.000
ring #2	175.5	173.6	1.011
ring #3	265.0	261.6	1.013
ring #4	357.0	348.8	1.024

2. Refractive Effect Corrections

The refractive distortion is caused by the difference in refractive index of the sample (n = 1.33) and the quartz

disks (n=1.5) comprizing the shear cell. This effect is a function of the inclination angle I of the shear cell with the respect to the incident beam and produces a distortion greater than the optical distortion discussed in the last section.

Figure (9) shows the trajectories followed by the incident and scattered light in the plane determined by the shear and velocity directions. Under ideal conditions with no refraction effects and no shear applied, the scattering pattern at any angle I must be spherically symmetric and a circular ring (first Debye-Scherrer ring) must be observed on the screen. However, because of the refraction, the observed scattering pattern is slightly distorted.

Let r1 and r3 represent the dimensions of the observed distorted ring. The distance r1 is shown in figure (9), the distance r3 is measured along the direction perpendicular to r1 and pointing out of the paper in figure (9). Using Snell's law, we obtained the following expression for r1:

$$r1 = \left[H1 - \frac{h1}{\cos(E)} \cos(E - I) \right] \tan(\theta) + \frac{h1}{\cos(E)} \sin(E - I)$$

$$+ \left[H1 - \frac{h1}{\cos(E_1)} \cos(I - E_1) \right] \tan(\theta) + \frac{h1}{\cos(E_1)} \sin(I - E_1) \qquad (3\text{-}4)$$

where

$$E \equiv \sin^{-1} \frac{1.33}{1.50} \sin(I + \theta) \qquad (3\text{-}5)$$

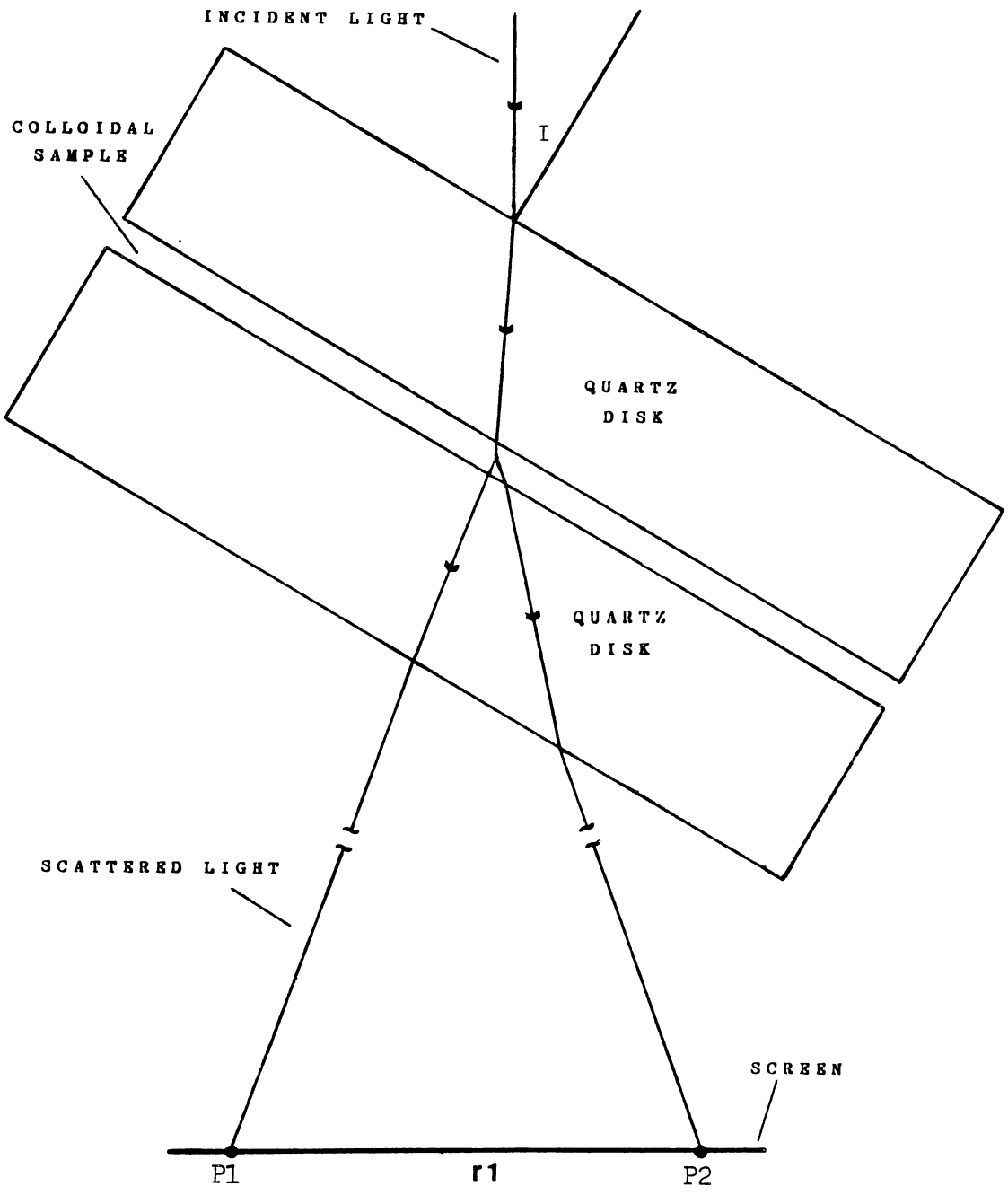

Figure 9. Ray Diagram Showing the Distortion due to Refraction Effects. The Distance r1 is a Function of the Scattering Angle I

$$E_1 \equiv \sin^{-1} \frac{1.33}{1.50} \sin(I - \theta) \qquad (3\text{-}6)$$

I is the angle of inclination of the shear cell respect to the incident beam and θ is the scattering angle, with respect to the incident beam. The distances h1 and H1 are the thickness of the quartz disk and the distance from the scattering volume to the screen, respectively.

If the axis of rotation of the shear cell coincides exactly with the position of the scattering volume when the cell is perpendicular to the incident beam ($I=0^{o}$), then the expression for r1 given in equation (3-4) must be an even function of I as shown by the line with the circles in figure (10). The line with the squares are the measured values of r1. These data were obtained by rotating the shear cell (with no shear applied) from -60^{o} to $+60^{o}$. Note that the calculated and measured values display a similar behavior except that the graph representing the measured values is not centered at the origin ($I=0^{o}$). This is an indication of an alignment effect made during the initial set up of the shear cell. The axis of rotation of the shear cell does not coincide exactly with the position of the scattering volume at $I = 0^{o}$.

When the sample is sheared, the scattering angle measured along the line of maximum distortion increased from approximately 20.7^{o} at a shear rate $w = 0\ sec^{-1}$ to 22.7^{o} at a shear rate $w = 9\ sec^{-1}$. It can be seen that the increase in the scattering angle $\Delta\theta$ caused by the shear is much smaller

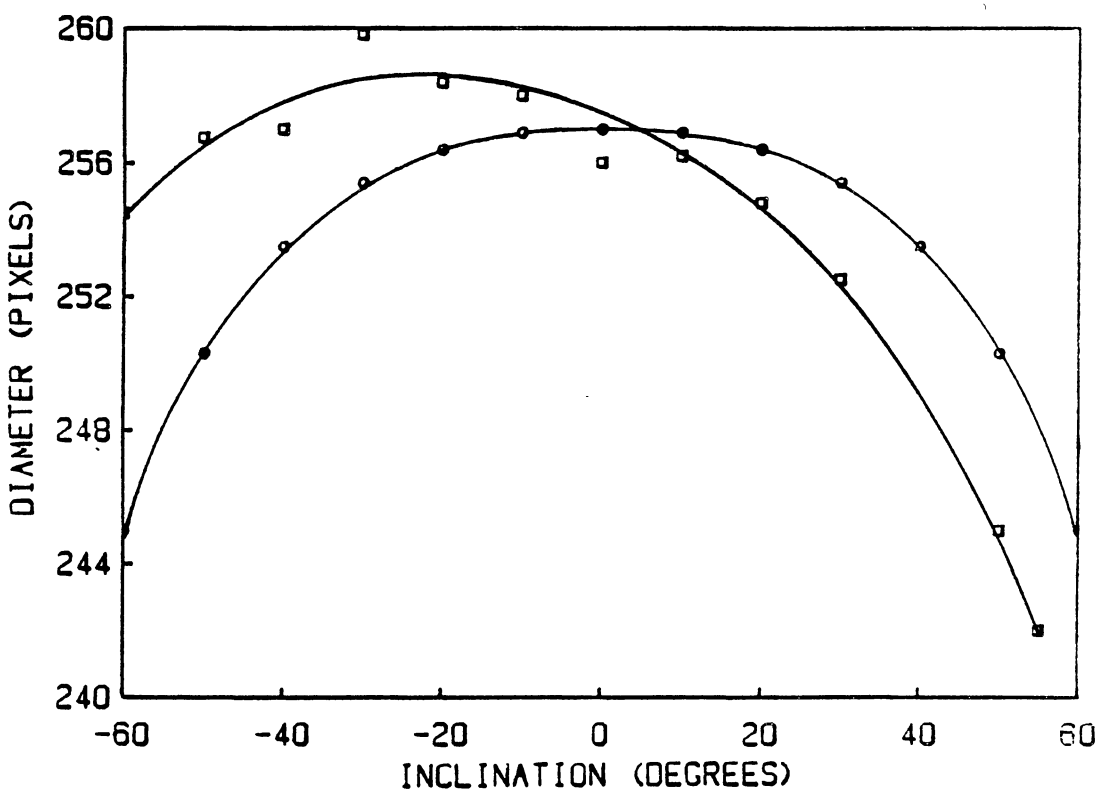

Figure 10. Variation of the Diameter of the Observed Debye-Scherrer Ring due to Refractive Effects. The Sample is not Sheared, the Measurements are Along the Line Determined by the Plane of the Viewing Screen and the Plane Containing the Velocity and Velocity Gradient Vectors
o o o Calculated Values
□ □ □ Measured Values

than the scattering angle θ measured at equilibrium ($\Delta\theta/\theta$ = Δ pixel count/pixel count < .01). If the sheared sample is rotated as described above, the observed dimensions of the scattering pattern contains both the distortion introduced by the shear effect and the distortion introduced by the refractive effect. One alternative is to correct individual measurements for refractive effects using equation (3-4). Another alternative is to express the measured data as relative measurement rather than absolute measurements. Although the diameter of the scattered ring r1(w,I) is a complicated function of the inclination angle I, the ratio r1(w,I)/r1(0,I) is found to be practically independent of I as long as $\Delta\theta << \theta$ (i.e. if the distortion caused by the shear is small compared with the equilibrium values). In figure (11) we show the calculated values of r1($\Delta\theta$,I)/r1(0,I) as a function of the angle of inclination. The lines with the black circles, squares, triangles, crosses and open circles represent a value of $\Delta\theta$ of 0, .6, 1.2, 1.8 and 2.4 degrees, respectively. It can be observed from the graph that for $\Delta\theta << \theta$, the refractive distortion are practically independent of the inclination angle I. In the worse case ($I = 60^{\circ}$ and $\Delta\theta = 2.4^{\circ}$) the error is .17%. We want to point out that the graph in figure (11) tells us the validity of the approximation that r1($\Delta\theta$,I)/r1(0,I) is independent of the angle I. The calculations are based on a sphere of diameter r1($\Delta\theta$,I); although the scattering pattern of a sheared system is not circular but ellipsoidal the results obtained are

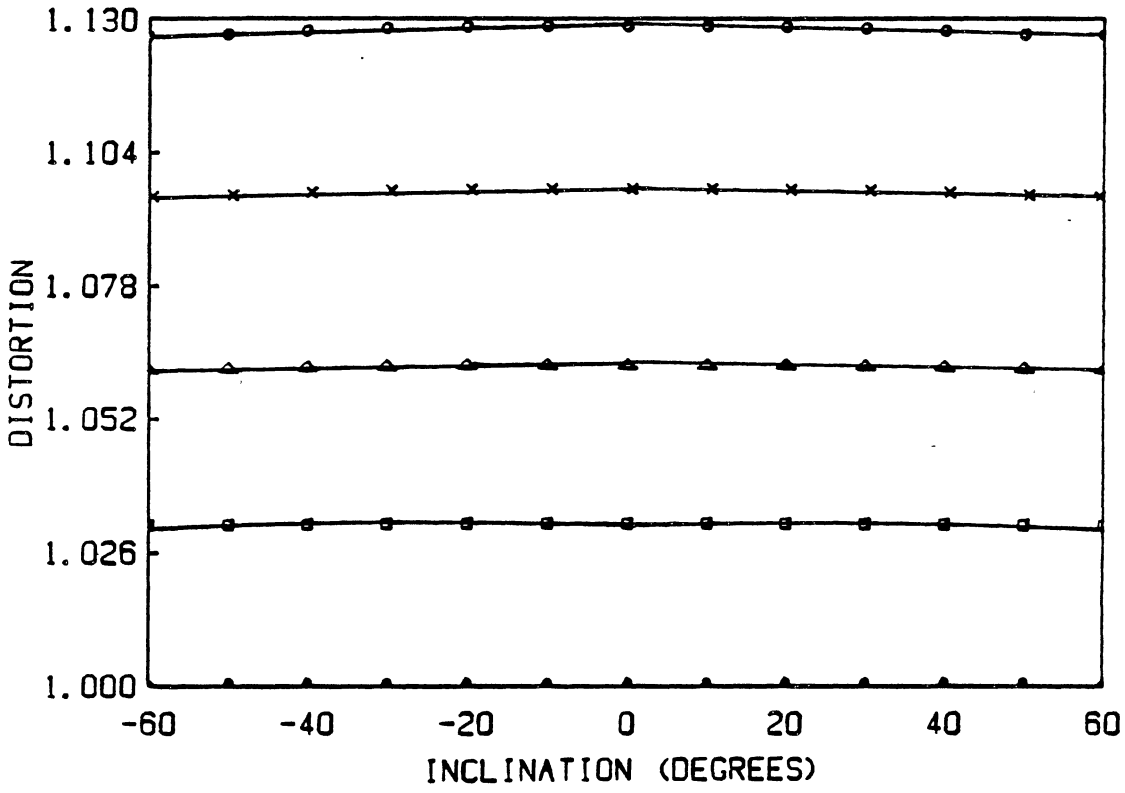

Figure 11. Refractive Effect Corrections Assuming Spherical Scattering Patterns of Different Scattering Angles θ
• • • 20.7°, □ □ □ 21.3°, ▲ ▲ ▲ 21.9°,
x x x 22.5°, o o o 23.1°

valid as long as the dimensions of the ellipsoid do not exceed the values of r1 shown in figure (11).

Another difficulty created by the inclination of the shear cell is that the intensity observed at point P2 is less than the intensity observed at point P1 (see figure (10)). This intensity variation is due to the following reasons:

a. Absorption by the colloidal sample (the light reaching point P2 travels a greater distance through the sample than the light reaching point P1)

b. Attenuation due to reflection (the angle of incidence on the quartz interface of the light reaching point P2 is greater than the angle of incidence of the light reaching point P1, consequently the transmission coefficients are different).

3. Other Corrections

Since we are using a flat photographic screen the observed intensity patterns $I(\bar{k})$ will be proportional to $I(\bar{k})\cos^2(\theta)$, where θ is the scattering angle. For the two samples analyzed, the scattering angle corresponding to the first Debye-Scherrer ring changed from approximately 21° at equilibrium to 23° at a shear rate of 9 sec^{-1} , consequently the scattering angle remained relatively constant and this correction for the intensity is negligible (in the worse case the error in the intensity is 2.8%).

Single scattering implies that after the encounter between the incident beam and a particle, the scattered

radiation proceeds directly to the detector without any further scattering encounter. In the laboratory, the necessary conditions for single scattering can be attained by working with dilute systems and with small volumes. With a sample of approximately 1 mm in thickness and a solid concentration of .17% multiple scattering is not entirely negligible and complicates any quantitative measurement of intensity.

The effect of a small gap in the rheological properties of charged particles have been investigated by Strivens (8). He found that the size of the gap has no effects as long as the gap exceeds some 250 times the average particle diameter. In our investigations the size of the gap is over 4000 times larger than the particle diameter, consequently we consider the effect of the size of the gap on the rheological properties of the sample to be insignificant.

CHAPTER IV

EXPERIMENTAL RESULTS AND COMPARISON WITH THE THEORY

The structure factor of two different colloidal particle samples undergoing shear flow was analyzed as a function of the applied shear rate. The samples are described on page 25. Three different properties were investigated during this research:

1) Radial displacement (in Fourier space) of the maximum in the Debye-Scherrer ring with respect to the equilibrium value as a function of the rate of shear.

2) Effect of the rate of shear on the maximum intensity of the first Debye-Scherrer ring.

3) Rotation of the ellipsoid of distortion of the first Debye-Scherrer ring as a function of the applied shear.

A. Experimental Results

1. Distortion of the Structure Factor as a Function of the Rate of Shear

This analysis consists in investigating the dimensions of the first Debye-Scherrer ring (i.e., value of r1 , r2 and r3) as a function of the shear rate. The physical meaning of r1, r2 and r3 is explained in page 34 and

illustrated in figure (7).

To measure the effect of the applied shear on the distances r1 and r3 the shear cell is oriented at -45° with respect to the incident laser beam and the shear rate was increased from 0 to approximately 10 sec^{-1} . Following a similar procedure but with the shear cell at $+45^{\circ}$ with respect to the incident beam, we obtain a measure of r2 and r3 . Figure (1) and figure (12) correspond to the observed scattering pattern when the shear cell is at -45° and $+45^{\circ}$, respectively. During all these measurements the shear cell is in configuration 1 (see page 32).

Since for these measurements the shear cell is at $\pm 45^{\circ}$ with respect to the incident beam, it is important to take into account the refraction problem. All the data reported in this section was corrected for refractive effects using the procedure discussed on page 39.

Figure (13) shows the average measured values when the shear cell is at -45° with respect to the incident laser beam. This data correspond to sample A; the line with the circles corresponds to the ratio r1(w)/r1(0) where r1(0) and r1(w) are the dimensions of the Debye-Scherrer ring at maximum intensity, along the R1 direction, when the sample is at equilibrium and undergoing shear flow, respectively. The shear rate is denoted by w. The line with the squares corresponds to the ratio r3(w)/r3(0); consequently, these two graphs show how the spherical scattering pattern at equilibrium is distorted along the $\hat{R}1$ and $\hat{R}3$ direction. An

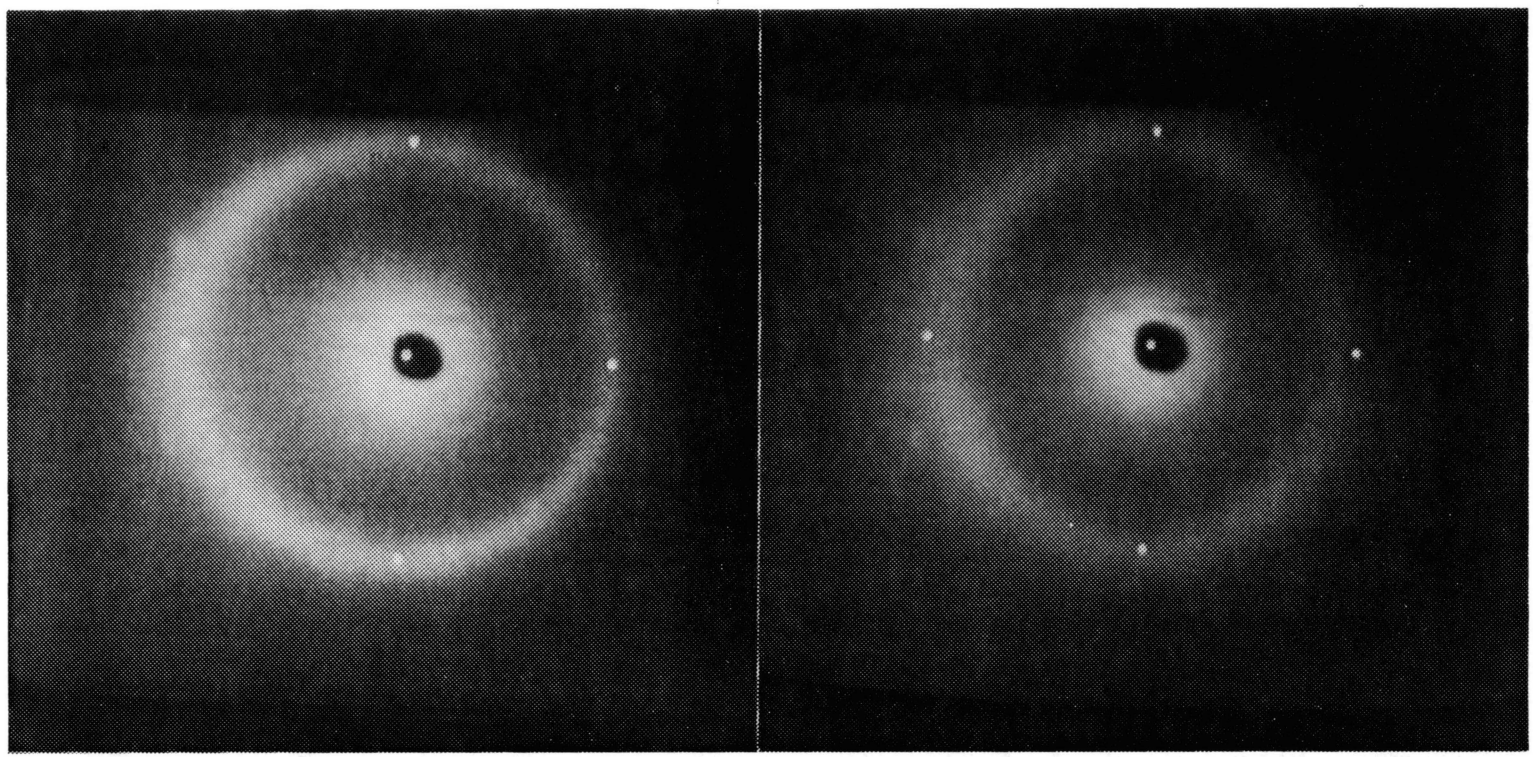

Figure 12. Observed Scattering Pattern of Dilute Colloidal Liquids When the Shear Cell is in the Configuration 1 Described in Page (32) and at +45° with Respect to the Incident Beam (a) Sample in Equilibrium (b) Sample Undergoing Shear

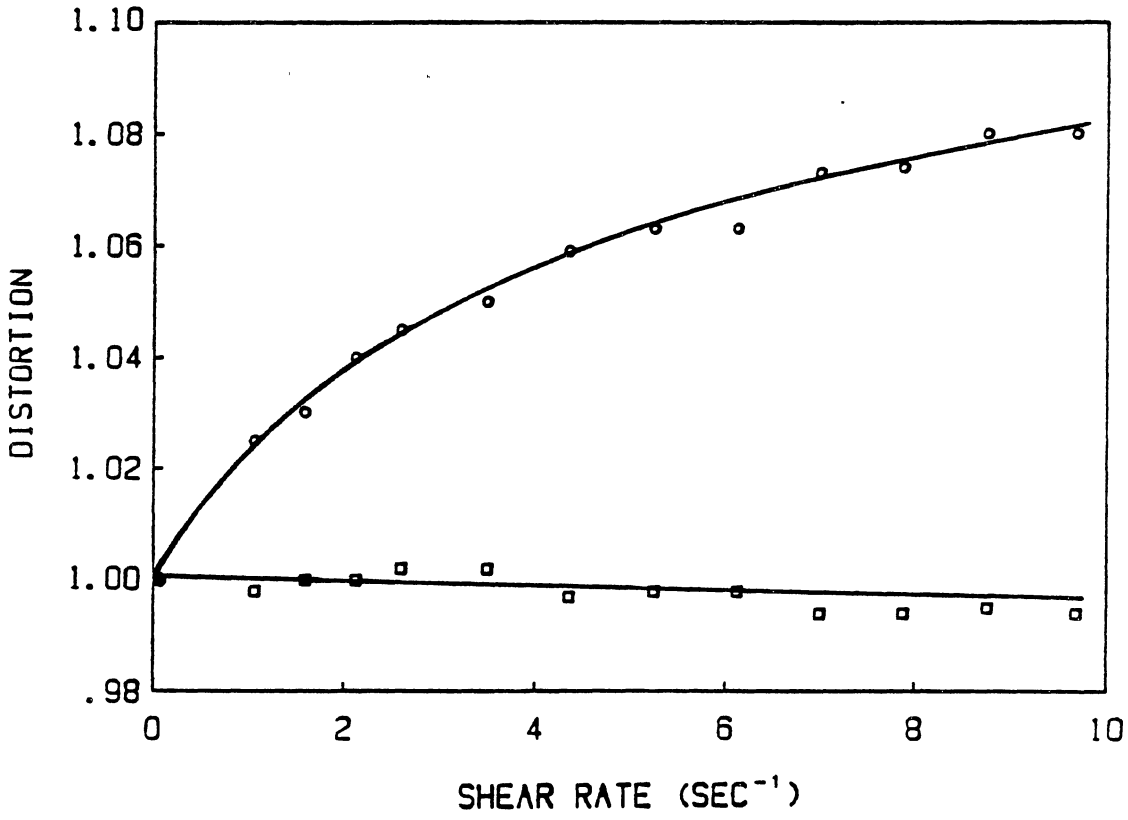

Figure 13. Measured Distortion of the Scattering Pattern of Sample A Along the Directions R1 and R3 as a Function of the Applied Shear Rate w
o o o r1(w)/r1(0) □ □ □ r3(w)/r3(0)

inspection of this graph shows that the distance r3 decreases slightly and that the distance r1 shows a nonlinear increase with the applied shear in contrast to earlier measurements reported by Ackerson and Clark (2). Figure (14) is similar to figure (13) except that now the distortion is plotted as a function of the square root of the shear rate rather than the shear rate. From figure (14) it is evident that r1 increases directly proportional with the square root of the shear rate. The small variation observed on r3 may be due to slight misalignment of the shear cell, such that the axis of rotation does not coincide with the position of the scattering volume when the incident beam is perpendicular to the shear cell.

Figure (15) shows the average measured distortion when the shear cell is at $+45^{\circ}$ with respect to the incident laser beam. This data corresponds to sample A; the line with the circle and the squares corresponds to the ratios r2(w)/r2(0) and r3(w)/r3(0), respectively. Note that the distortion along the $\hat{R}3$ direction is very similar to the one obtained previously; this must be the case since we are looking at the same dimension in this orientation. The main difference is that the distance r2 shows a non linear decrease with the applied shear. Figure (16) shows these distortions plotted as a function of the square root of the rate of shear. From this graph it is evident that there is a linear relationship between the decrease in r2 and the square root of the shear rate.

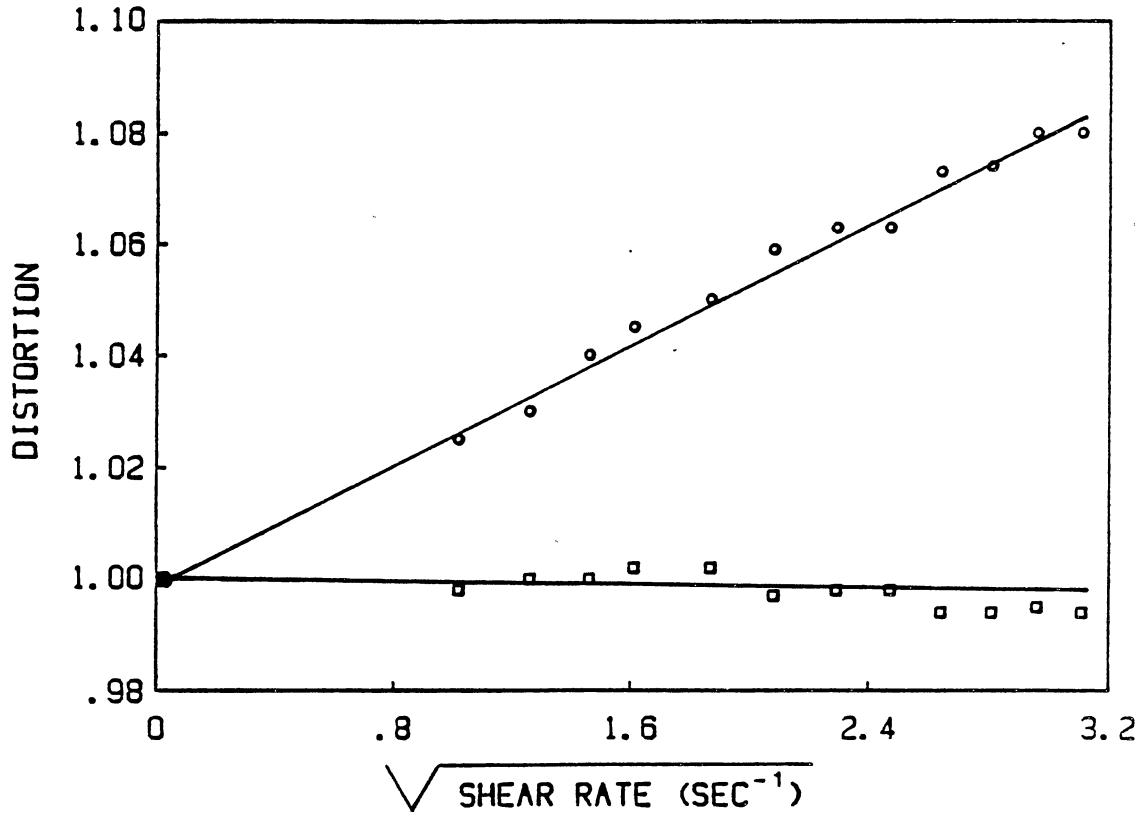

Figure 14. Measured Distortion of the Scattering Pattern of Sample A Along the Directions R1 and R3 as a Function of the Square Root of the Applied Shear Rate w
o o o r1(w)/r1(0) □ □ □ r3(w)/r3(0)

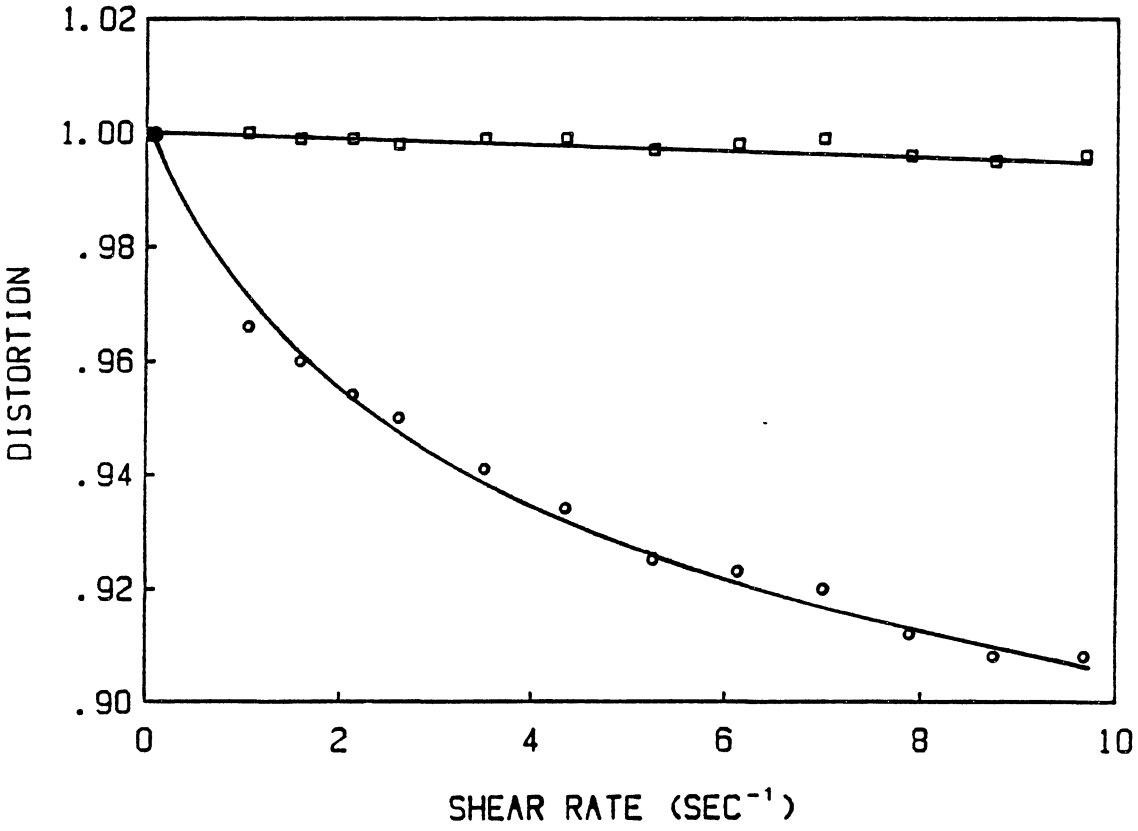

Figure 15. Measured Distortion of the Scattering Pattern of Sample A Along the Directions R2 and R3 as a Function of the Applied Shear Rate w
o o o r2(w)/r2(0) □ □ □ r3(w)/r3(0)

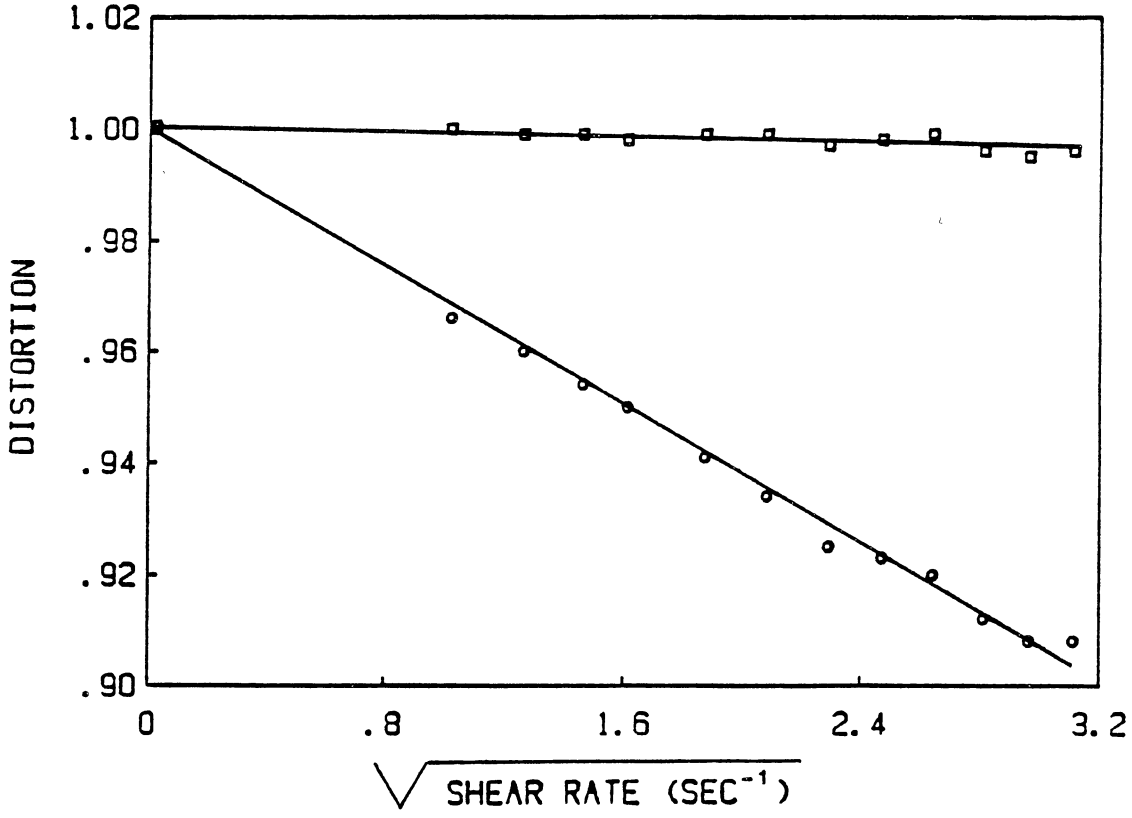

Figure 16. Measured Distortion of the Scattering Pattern of Sample A Along the Directions R2 and R3 as a Function of the Square Root of the Applied Shear Rate w
o o o r2(w)/r(0) □ □ □ r3(w)/r3(0)

Combining the information provided from figure (13) and figure (16) we conclude that the spherical structure factor at equilibrium degenerates into a distorted ellipsoid when a shear is applied. The dimensions of this ellipsoid are r1,r2 and r3 with r1> r3> r2.

Similar analysis were performed using sample B. Figure (17) shows the average measured values when the shear cell is at -45 with respect to the incident laser beam. The lines with the circles and squares correspond to r1(w)/ r1(0) and r3(w)/r3(0), respectively. Figure (18) shows these distortions as a function of the square root of the rate of shear.

A comparison of figure (13) and figure (14) with figure (17) and figure (18) show that both samples behave very similar when a shear is applied; the main differences are that in sample B the distance r3 remains relatively constant and that the graph in figure (18) does not extrapolate to 1 at zero shear rate.

2. Effect of the Rate of Shear on the Peak Intensity of the Debye-Scherrer Ring

In this analysis we investigate how the peak intensity along the directions $\hat{R}1$, $\hat{R}2$ and $\hat{R}3$ change, when the sample is undergoing shear flow.

Figure (19) and figure (20) show the measured average intensity for two different shear rates, the solid and broken lines correspond to a sample in equilibrium and undergoing a

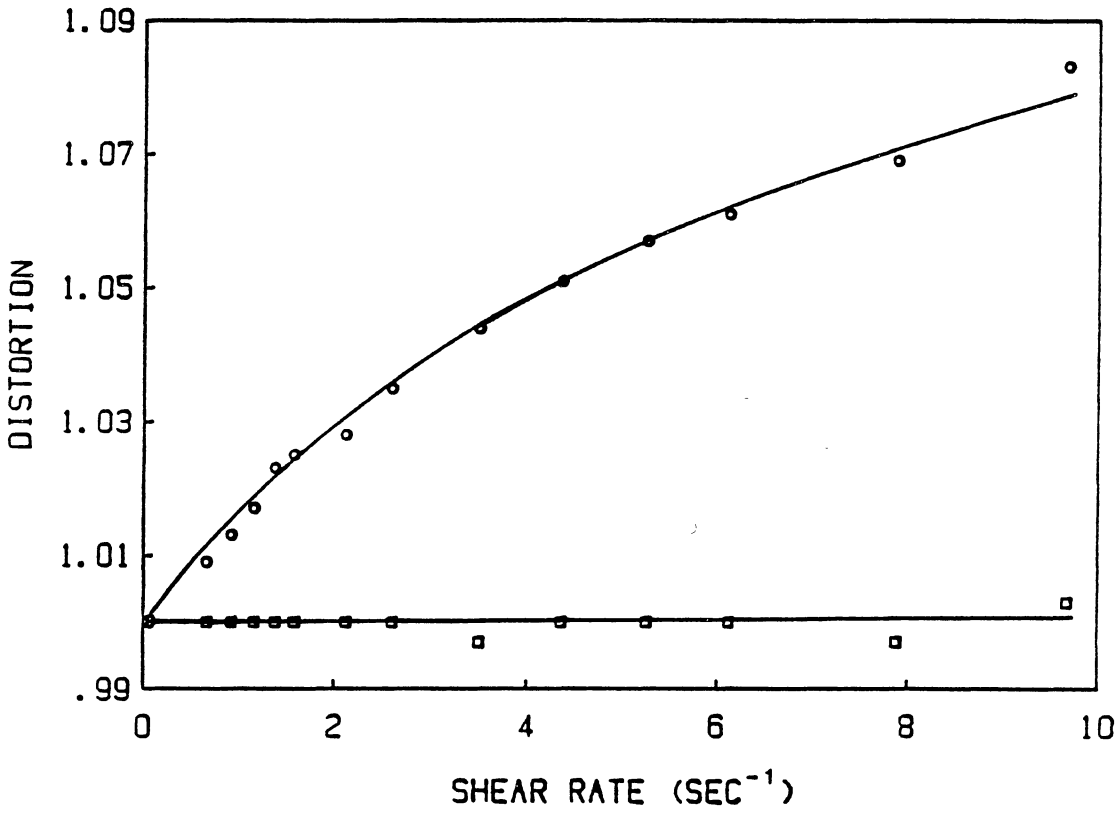

Figure 17. Measured Distortion of the Scattering Pattern of Sample B Along the Directions R1 and R3 as a Function of the Applied Shear Rate w
o o o r1(w)/r1(0) □ □ □ r3(w)/r3(0)

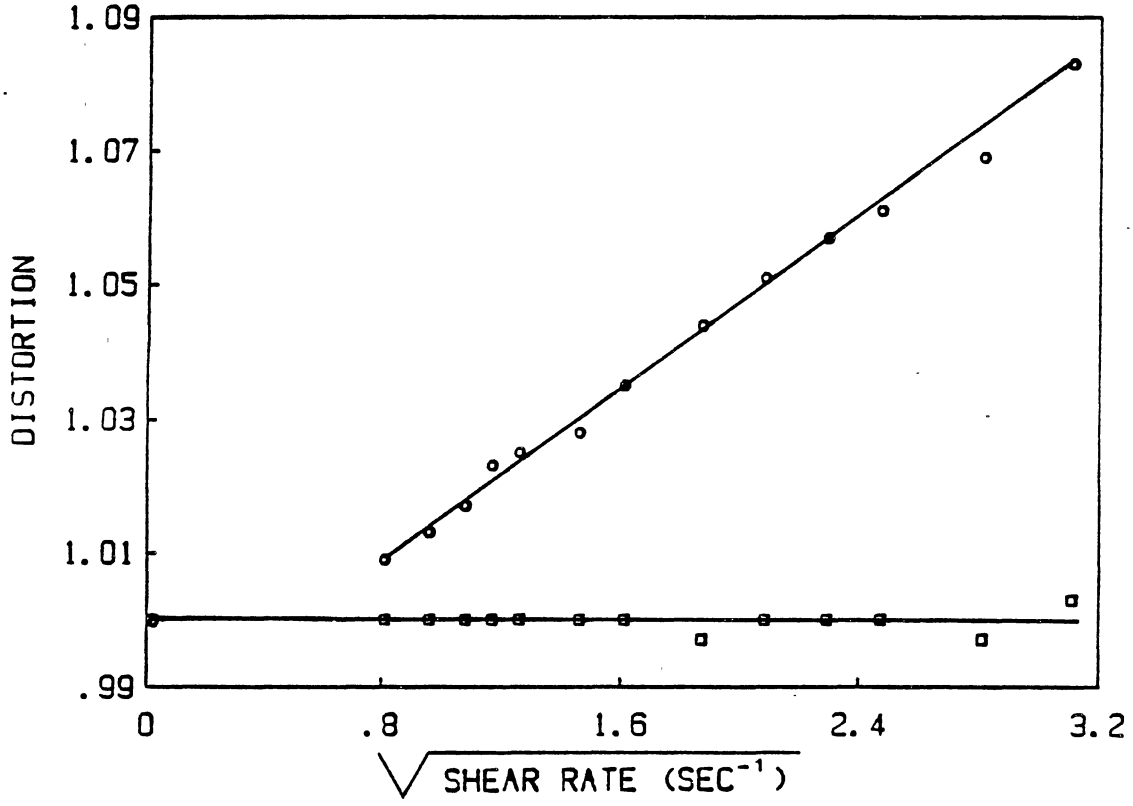

Figure 18. Measured Distortion of the Scattering Pattern of Sample B Along the Directions R1 and R3 as a Function of the Square Root of the Applied Shear Rate w
o o o r1(w)/r1(0) □ □ □ r3(w)/r3(0)

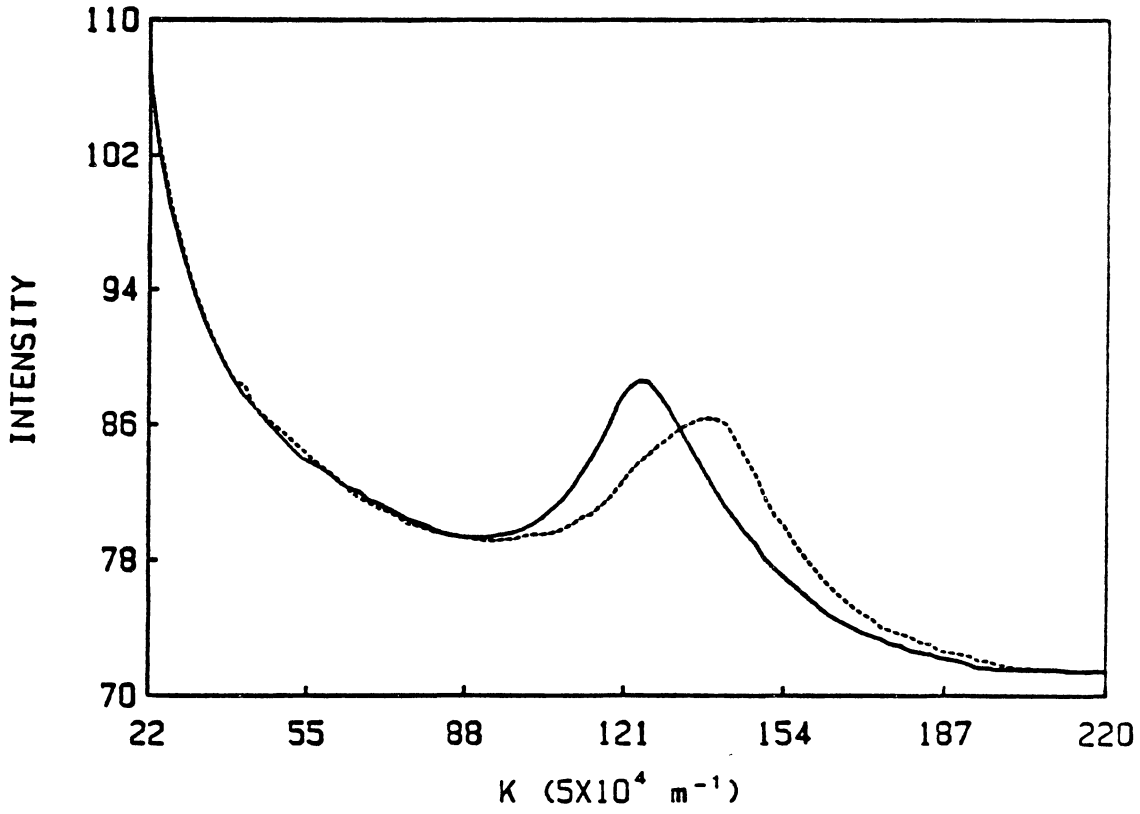

Figure 19. Measured Average Intensity Along the Direction R1 for two Different Shear Rates w. The Peak Near the Origin Corresponds to Stray Light from the Incident Laser Beam
—— w = 0 sec^{-1} ---- w = 9 sec^{-1}

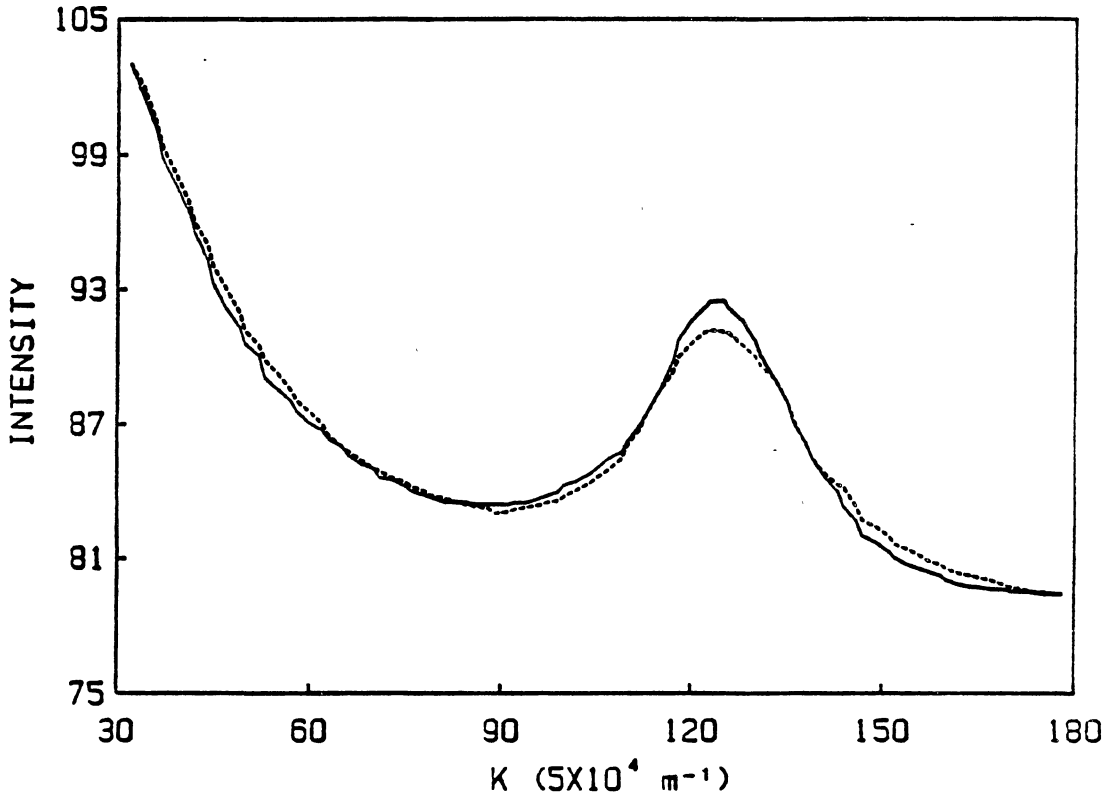

Figure 20. Measured Average Intensity Along the Direction R3 for two Different Shear Rates w. The Peak Near the Origin Corresponds to Stray Light from the Incident Laser Beam
—— w = 0 sec^{-1} ---- w = 9 sec^{-1}

shear of 9 sec^{-1}, respectively. This data was taken with the shear cell at -45^{o} with respect to the incident laser beam, consequently figure (19) and figure (20) are a scan of the intensity along the $\hat{R}1$ and $\hat{R}3$ directions, respectively. To investigate the intensity variations along the $\hat{R}2$ direction the shear cell is inclined at $+45^{o}$ with respect to the incident laser beam, the measured intensity along the $-\hat{R}2$ direction is shown in figure (21). The intensity is measured along the $-\hat{R}2$ rather than the $+\hat{R}2$ direction because the measured intensity along the $-\hat{R}2$ direction is larger than that obtained along the $+\hat{R}2$ direction. An explanation of this effect was given in page 46. Since low intensity signals are usually more noisy than high intensity signals, then there is a clear advantage of measuring the intensity along the $-\hat{R}2$ rather than the $+\hat{R}2$ direction.

The data shown in figure (19) to figure (21) correspond to sample A and the shear cell is in the configuration 1 shown in figure (6-a). The peak near the origin corresponds to stray light from the incident laser beam.

Note that there are several problems that must be solved before attempting to obtain numerical data relating the intensity with the shear rate. For example, it is known that the intensity response of some video cameras is not linear, similarly the intensity response of the video digitizer may not be linear. Since we do not have any technical information concerning this linearity effect, no corrections were made in this respect. Another problem that

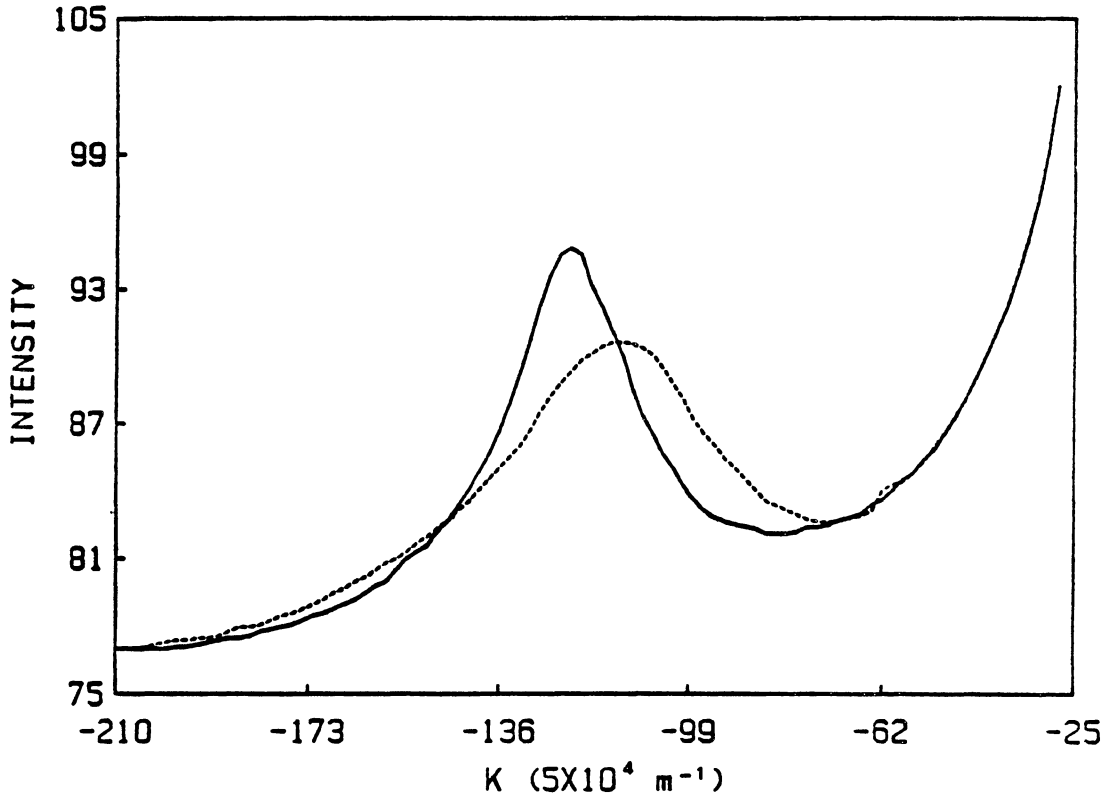

Figure 21. Measured Average Intensity Along the Direction -R2 for two Different Shear Rates w. The Peak Near the Origin Corresponds to Stray Light from the Incident Laser Beam
—— w = 0 sec^{-1} ---- w = 9 sec^{-1}

can affect the observed intensity is that as we move away from the center of the viewing screen, the corresponding angles of incidence in the quartz interface are not constant giving rise to different transmission coefficients. A major problem is that the observed intensity is the sum of the "true" scattered light plus the stray light coming from the incident beam. To overcome this problem we begin by observing that some regions in the intensity plots, see figure (19), remain unchanged when the shear is applied; consequently, and estimation of the background intensity can be obtained by drawing a base line as illustrated in figure (22). The "true" scattered light can be obtained by subtracting the corresponding background intensity. Another problem related to the intensity measurements is the fact that we are using a flat viewing screen; consequently, as we move away from the origin, the distance r from the scattering volume to the screen increases. It is well known from elementary optics that the intensity decreases according to $1/r^2$, or in terms of the scattering angle θ as $1/\cos^2(\theta)$ for a constant collection area detector.

All our measurements were performed on the peak value of the intensity. From figure (22) it is clear that the variation of the scattering angle is very small (our calculations show that the scattering angle increases from approximately 21° at equilibrium to approximately 23° at a shear rate of 9 sec^{-1}). Under these conditions the intensity variations due to $1/\cos^2(\theta)$ are negligible (in the worse case

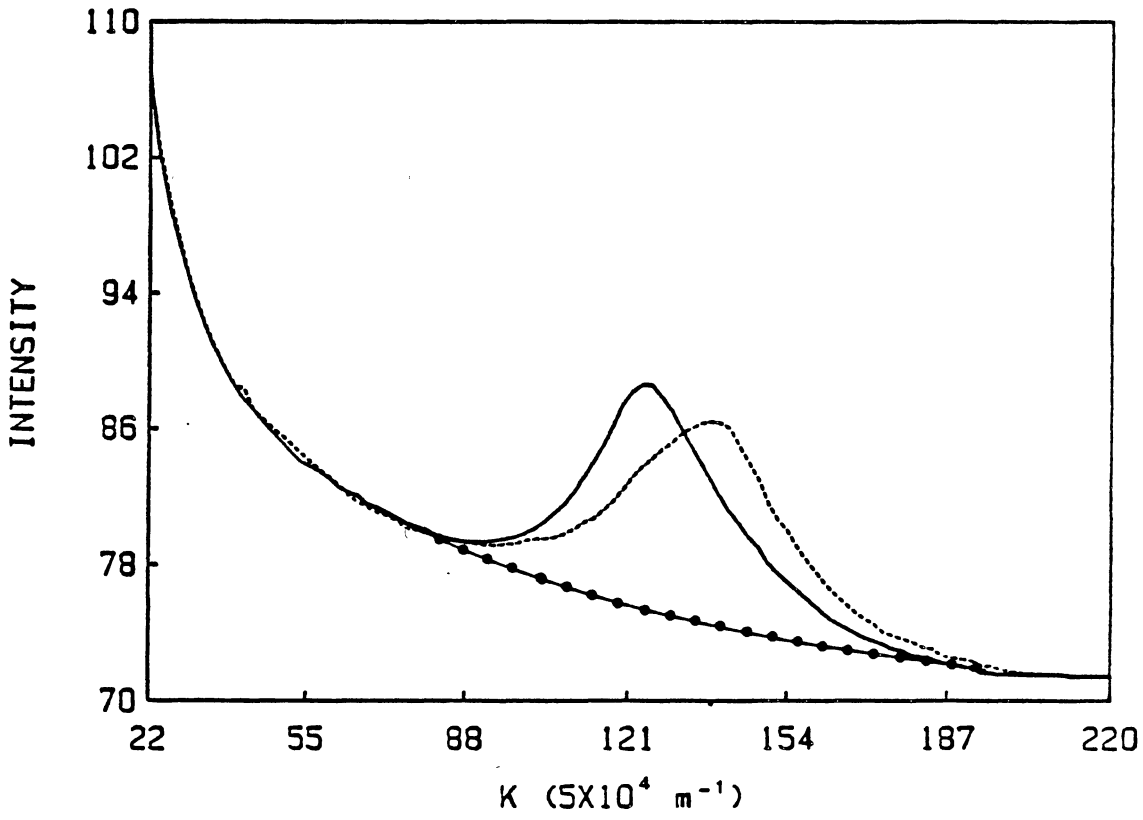

Figure 22. This Graph is Similar to the Graph Shown in Figure (19). The Additional Curve with the Circles was Used to Correct the Data from Background Intensity

the calculated error is 2.8%). Then the main problem is the background intensity. Figure (23) shows how the peak intensity along the $\hat{R}1$ direction changes as a function of the shear rate. The data shown corresponds to sample A and is corrected using the extrapolated background intensity criteria.

3. Rotation of the Ellipsoid of Distortion as a Function of the Applied Shear

As explained earlier, the spherical scattering pattern at equilibrium degenerates into a distorted ellipsoid when the colloidal liquid is sheared; the maximum and minimum distortion being along the $\hat{R}1$ and $\hat{R}2$ directions, respectively. Some theoretical calculations show that for small shear rates the direction of $\hat{R}1$ is at 45° with respect to the velocity gradient, but for high shear rates the direction of $\hat{R}1$ changes becoming closer to the direction of the velocity gradient.

The analysis presented in this section consists in determining how the orientation of the distorted ellipsoid in Fourier space changes as a function of the shear rate.

This analysis can be performed in two different ways:

a. One possibility is to set the shear cell as illustrated in configuration 1 (see figure (6-a)) and rotate the sheared sample slowly. This seems to be the logical approach, however a major problem with this technique is that the distortion introduced by the refraction is not

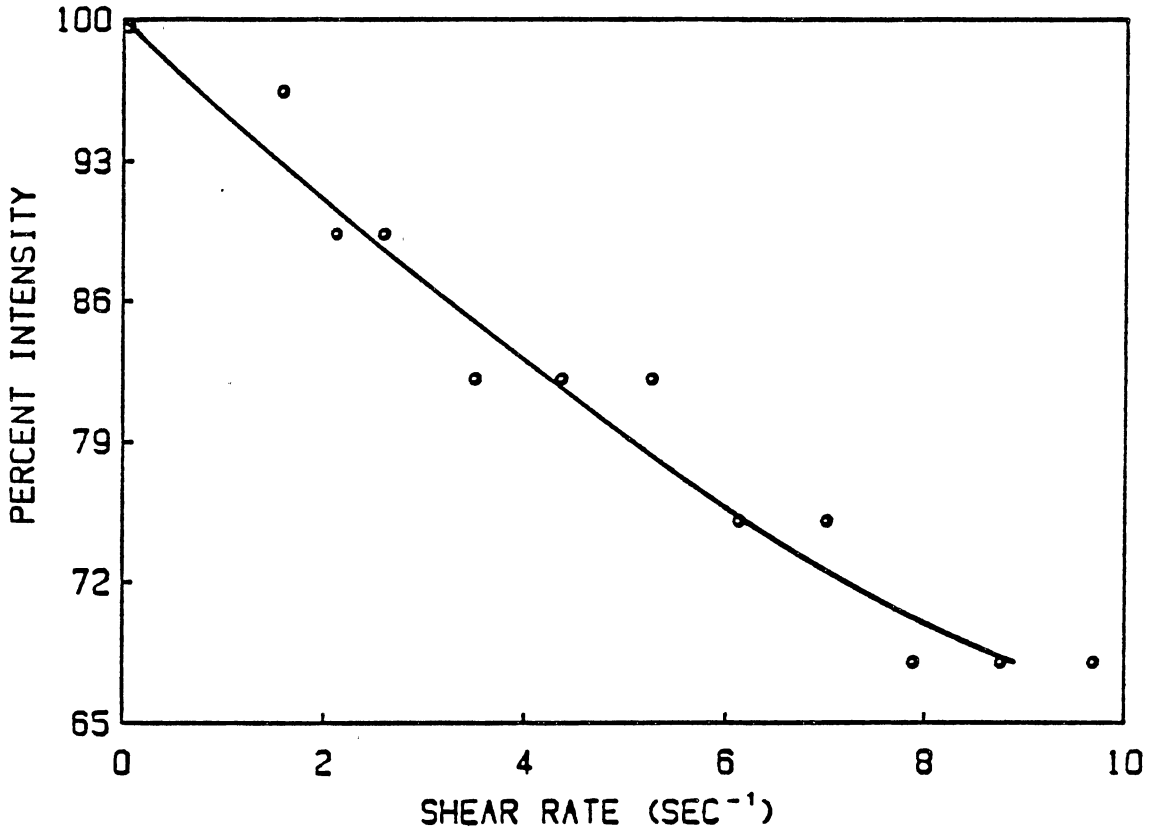

Figure 23. Measured Decrease in the Peak Intensity Along the Direction R1 as a Function of the Rate of Shear. These Data Correspond to Sample A, the Intensity is Corrected from Background as Explained in the Text

constant but a function of the inclination angle I.

b. Another possibility is to set the shear cell as illustrated in configuration 2 (see figure (6-b)) with an inclination angle I of 90° and increase the shear rate to see if any rotation of the major axis of the ellipse is observed. A difficulty with this technique is that the design of the shear cell allows a maximum rotation of 60°; consequently, it is impossible to project the major axis of the ellipsoid on the viewing screen.

In an effort to determine if the applied shear produces a change in the direction of $\hat{R}1$ and $\hat{R}2$ (i.e., a rotation of the ellipsoid) both techniques described above were used.

Figure (24) shows the data obtained when the shear cell is set as described in configuration 1, this figure shows the measured distortion as a function of the inclination angle I for three different shear rates. The measured values were corrected from refractive effects using the procedure discussed in page 39. The circles, squares and triangles correspond to shear rates of 1.85, 3.05 and 5.25 sec^{-1}, respectively. The distortion is defined as d(w,I)/d(0,I) where d(w,I) is the measured diameter of the first Debye-Scherrer ring; w and I are the shear rate and the inclination angle of the shear cell respect to the incident beam, respectively. The measurements of d(w,I) are in the plane containing the velocity and shear gradient vectors. The maximum near -50° corresponds to the major axis of the ellipse ($\hat{R}1$ direction); the minimum near +40° corresponds to

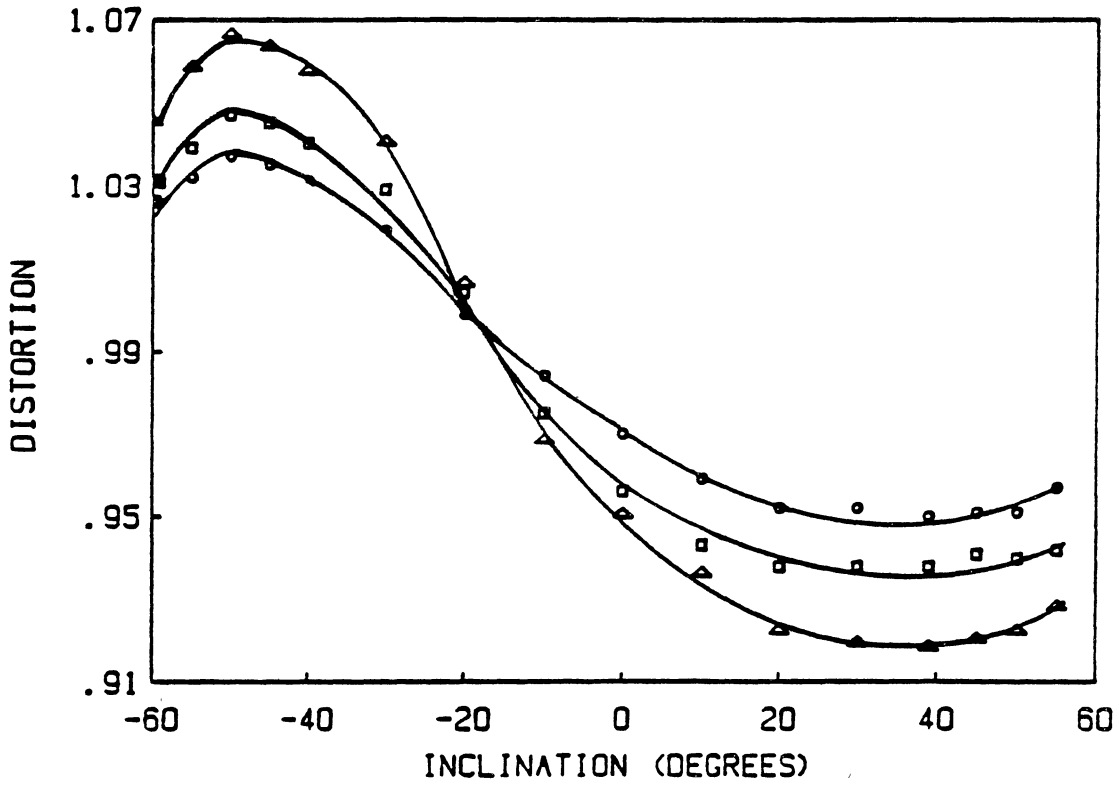

Figure 24. Measured Distortion of the Scattering Pattern of Sample A for Three Different Rates of Shear w
o o o w = 1.85 sec^{-1} □ □ □ w = 3.05 sec^{-1}
△ △ △ w = 5.25 sec^{-1}

the minor axis of the ellipse ($\hat{R}2$ direction). Note that the position of the maximum and the minimum remains approximately constant. This indicates that the shear is not producing any appreciable rotation of the scattering patterns at these shear rates. It should be pointed out that for a sample with a relaxation time of 8 ms undergoing a shear flow of 5.25 sec^{-1}, like the curve with triangles in figure (24), the Hess theory predicts that the minimum of the curve must be shifted to the right by approximately 1.2^{o}. Such a small rotation is difficult to measure experimentally; consequently higher shear rates or a different approach is necessary. The difficulty with higher shear rates is that for angles of inclination larger than 45^{o} the ring becomes to diffuse to get an accurate reading. Thus no data for shear rates larger than 5.25 sec^{-1} is plotted in figure (24).

Some analyses were performed with the shear cell set up as described in configuration 2 (see figure (6-a) with the shear cell rotated by 60^{o} about the y axis. The sample was sheared to a maximum shear rate of 40 sec^{-1} ; under these conditions the major effect is that the scattering pattern brakes up along the line of maximum distortion even though one may argue that there is a slight rotation of the major axis of the ellipse towards the direction of the velocity gradient.

B. Comparison of the Experimental Results with the Theory

At this point we proceed to compare the experimental results presented in the first part of this chapter with the theory presented in Chapter II.

The fact that for sheared samples the scattering pattern is distorted along a line at 45° with respect to the velocity gradient can be easily understood by looking at the properties of the stress tensor. The rheological properties of simple fluids undergoing a small flow velocity can be derived from the following form of the stress tensor (see eq. (A-6))

$$\overleftrightarrow{\sigma} = - p \overleftrightarrow{1} + 2 \eta \overleftrightarrow{\varepsilon} \qquad (4\text{-}1)$$

where p and η are the equilibrium pressure and coefficient of shear viscosity, respectively; $\overleftrightarrow{1}$ represents the unit tensor, the rate of strain tensor $\overleftrightarrow{\varepsilon}$ is defined as

$$\overleftrightarrow{\varepsilon} = 1/2 \ (\bar{\nabla} \bar{V} + \bar{\nabla} \widetilde{\bar{V}}) \qquad (4\text{-}2)$$

In our case the flow velocity is given by

$$\bar{V} = w \, x \, \hat{y} \qquad (4\text{-}3)$$

where w is the rate of shear, thus the tensor $\overleftrightarrow{\varepsilon}$ takes the form

$$\overleftrightarrow{\varepsilon} = w/2 \ (\hat{y} \, \hat{x} + \hat{x} \, \hat{y}) \qquad (4\text{-}4)$$

Using a cartesian basis and equation (4-4) we can represent the stress tensor $\overleftrightarrow{\sigma}$ in matrix as follows

$$(\sigma) = \begin{bmatrix} -p & \eta w & 0 \\ \eta w & -p & 0 \\ 0 & 0 & -p \end{bmatrix} \tag{4-5}$$

It is well known that any symmetric tensor can be brought into diagonal form by an orthogonal transformation. Let $\hat{R}1$, $\hat{R}2$ and $\hat{R}3$ represent the basis vectors of the coordinate system in which the stress tensor has a diagonal form. This new basis determines the principal axis of the stress tensor and corresponds to the direction of maximum and minimum stress. Following the standard procedure (29) we proceed to diagonalize the stress tensor. The eigenvalues are:

$$\lambda_1 = -p - \eta w \tag{4-6a}$$

$$\lambda_2 = -p + \eta w \tag{4-6b}$$

$$\lambda_3 = -p \tag{4-6c}$$

The corresponding normalized eigenvectors are:

$$\hat{R}1 = 1/\sqrt{2} \begin{bmatrix} 1 \\ -1 \\ 0 \end{bmatrix} \tag{4-7a}$$

$$\hat{R}2 = 1/\sqrt{2} \begin{bmatrix} 1 \\ 1 \\ 0 \end{bmatrix} \tag{4-7b}$$

$$\hat{R}3 = \begin{bmatrix} 0 \\ 0 \\ 1 \end{bmatrix} \qquad (4\text{-}7c)$$

Note that this new basis is obtained by rotating the original basis about the z axis by 45° . This indicates that when the sample is undergoing shear flow according to equation (4-3) the directions of maximum and minimum stress are at $+45^{\circ}$ and -45° with respect to the velocity gradient.

Before we proceed to compare our experimental results with the theory, we want to point out that the theories presented in Chapter II relate the nonequilibrium structure factor $S(\bar{k},w)$ with the equilibrium value $S(k,0)$. This implies that we must have an accurate value of $S(k,0)$. From the data shown in figures (19) to figure (21) it is evident that there are severe experimental difficulties that prevent an accurate measurement of $S(k,0)$; the main problem is stray light from the incident beam near the $k=0$ region. In the absence of an accurate experimental value of $S(k,0)$ several models have been proposed, among others are the linear chain of harmonically coupled particles (5) and a hypernetted chain (HNC) model (6). Our comparison with the theory will be based on these two models.

1. Comparison of the Experimental Results with the Theory Based on the Stoke's Model

According to this theory the nonequilibrium structure factor $S(\bar{k},w)$ is related to the equilibrium value $S(k,0)$ by the following equation:

$$S(\bar{k},w) = S(k,0) - \tau w \frac{k_x k_y}{k} \frac{dS(k,0)}{dk} \qquad (4\text{-}8)$$

To see how well this theory compares with our experimental data the last equation was evaluated numerically. The equilibrium value S(k,0) was calculated using the linear chain model (5).

$$S(k,0) = \frac{1 - \exp\ (-k^2/(2\alpha\beta)}{1 + \exp\ -k^2/(2\alpha\beta)\ - 2\cos(ka)\exp\ (-k^2/(4\alpha\beta)} \qquad (4\text{-}9)$$

where a is the spacing between the colloidal particles, α is the coupling constant and $\beta \equiv 1/k_b T$. The value of a, and $\alpha\beta$ was chosen in such a way that the calculated structure factor resembles the measured value.

The solid line in figure (25) represents the value of S(k,0) calculated using equation (4-9) with $a = 9.9X10^{-7}$ m and $\alpha\beta = 6.5X10^{12}$ $1/m^2$. Using this equilibrium value, equation (4-8) was evaluated numerically. The calculated nonequilibrium values along the direction $\hat{R}1$ are represented by the broken line in figure (25), a value of $\tau w = .2$ was used for the calculations. A comparison of figure (25) with figure (19) indicate that this theory predicts the distortion of $S(\bar{k},w)$ observed experimentally; however, this theory cannot explain the decrease in the peak value of $S(\bar{k},w)$ observed experimentally. In fact this theory in this form predicts an increase in the peak value of $S(\bar{k},w)$ rather than a decrease.

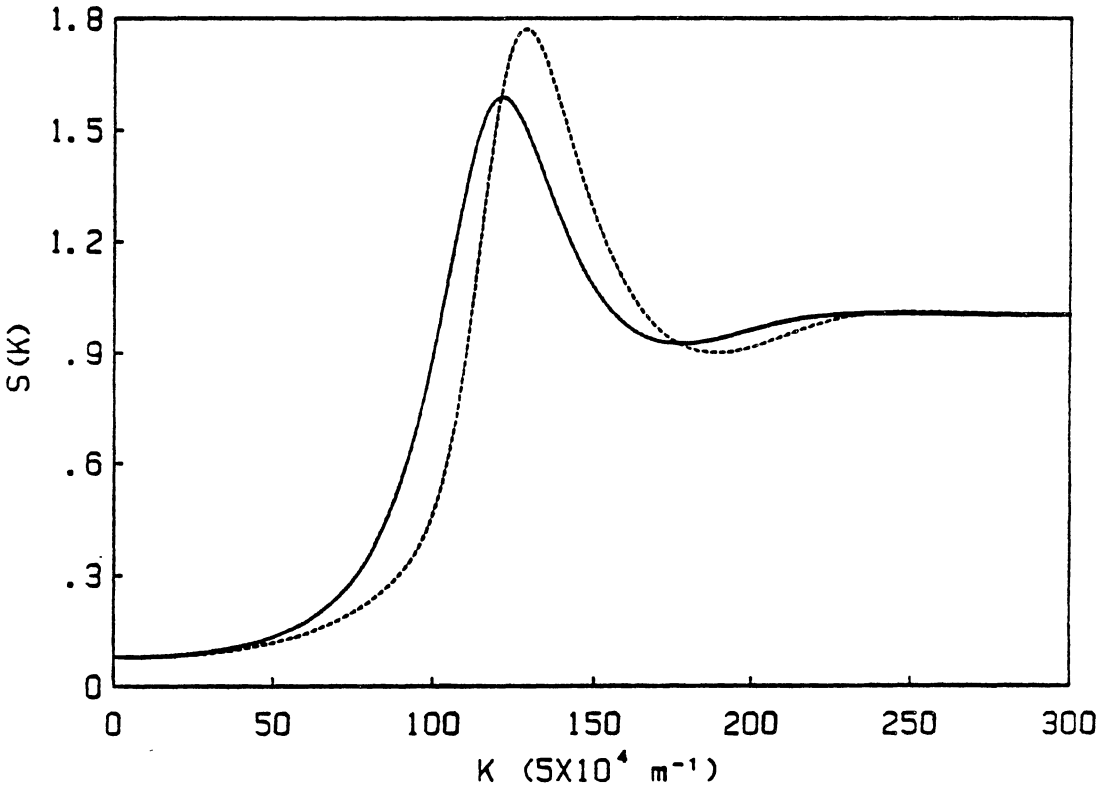

Figure 25. Calculated Structure Factor Using a Model of a Linear Chain of Harmonically Coupled Particles, the Values are Calculated Along the Direction R1
—— Equilibrium Values
---- Nonequilibrium Values

The reason why this theory breaks down near the peak value of $S(\bar{k},w)$ is that equation (4-8) can be considered as a power expansion in the shear rate w truncated to first power. Since this equation is valid for small flow velocities only; the linear term in w involves the first derivative of $S(k,0)$ which is very small or zero near the maximum of $S(k,0)$. This implies that the higher order terms neglected in equation (4-8) becomes the dominant in this range and have to be taken into account.

According to this theory the spherical scattering pattern at equilibrium will degenerate into an ellipsoid when the colloidal liquid is sheared. The major and minor axis of the ellipse (distance along $\hat{R}1$ and $\hat{R}2$) are at -45° and $+45^{\circ}$ with respect to the velocity gradient. This theory correctly predicts that no distortion will be observed along the $\hat{R}3$ direction. An alternate expression of this theory (see equation (2-21)) indicates no change of the maximum intensity as a function of shear, an ellipsoidal distortion which is linear in the shear rate, and no rotation of the ellipse of distortion as the shear increases. The first two results disagree with experimental observations and the last is only qualitatively correct, as this theory predicts zero distortion at $I = 0^{\circ}$ in figure (24) and not at $I = -20^{\circ}$.

2. Comparison of the Experimental Results with the Theory of Hess

As explained in Chapter II, the major improvement of this theory over the previous one is that it predicts a rotation of the scattering pattern with respect to the 45° direction predicted by the theory based on the Stoke's model.

Although this rotation cannot be detected in the low shear rate data plotted in figure (24), some analyses conducted at a shear rate of 40 sec^{-1} seems to indicate a slight rotation of the scattering pattern or a brake up of the pattern evidencing more solid-like order.

3. Comparison of the Experimental Results with the Theory of Ronis

According to this theory the nonequilibrium structure factor $S(\bar{k},w)$ is related to the equilibrium value $S(k,0)$ by the following equation

$$S(\bar{k},w) = \frac{2Ds}{|k_y w|} \int_L^{\infty} d\tilde{k}_x (\tilde{k}_x^2 + k_y^2 + K_z^2) \exp(-A)$$

$$A \equiv \frac{2Ds}{|k_y w|} \int_L^{\tilde{k}_x} dx \frac{(x^2 + k_y^2 + k_z^2)}{S(x,0)} \qquad L \equiv \frac{k_x k_y w}{|k_y w|} \qquad (4\text{-}10)$$

A Fortran program, listed in Appendix B, was written to integrate equation (4-10) numerically. Two different model equilibrium values $S(\kappa,0)$ were used during the calculations.

The first one, based on the HNC model, was obtained directly from the calculations reported by Ronis (6). The purpose of using this equilibrium value was mainly to compare the output of the Fortran program with the results reported by Ronis; in other words to test the validity of the computer program.

The results of the calculations are shown in figure (26); the line with the circles represents the equilibrium structure factor $S(k,0)$, the line with the triangles represents the calculated nonequilibrium factor $S(\bar{k},w)$ along the direction of maximum distortion R1 for a shear rate of 10 sec^{-1}.

A comparison of figure (26) with figure (19) shows that the distortion and decrease in the peak value of the nonequilibrium structure factor can be explained with this theory. Similar to the two theories discussed earlier, this theory predicts that the spherical scattering pattern observed at equilibrium will degenerate into a distorted ellipsoid when the colloidal liquid is sheared. The major and minor axis of the ellipse are at -45° and $+45^{\circ}$ with respect to the velocity gradient and no distortion observed along the $\hat{R}3$ direction.

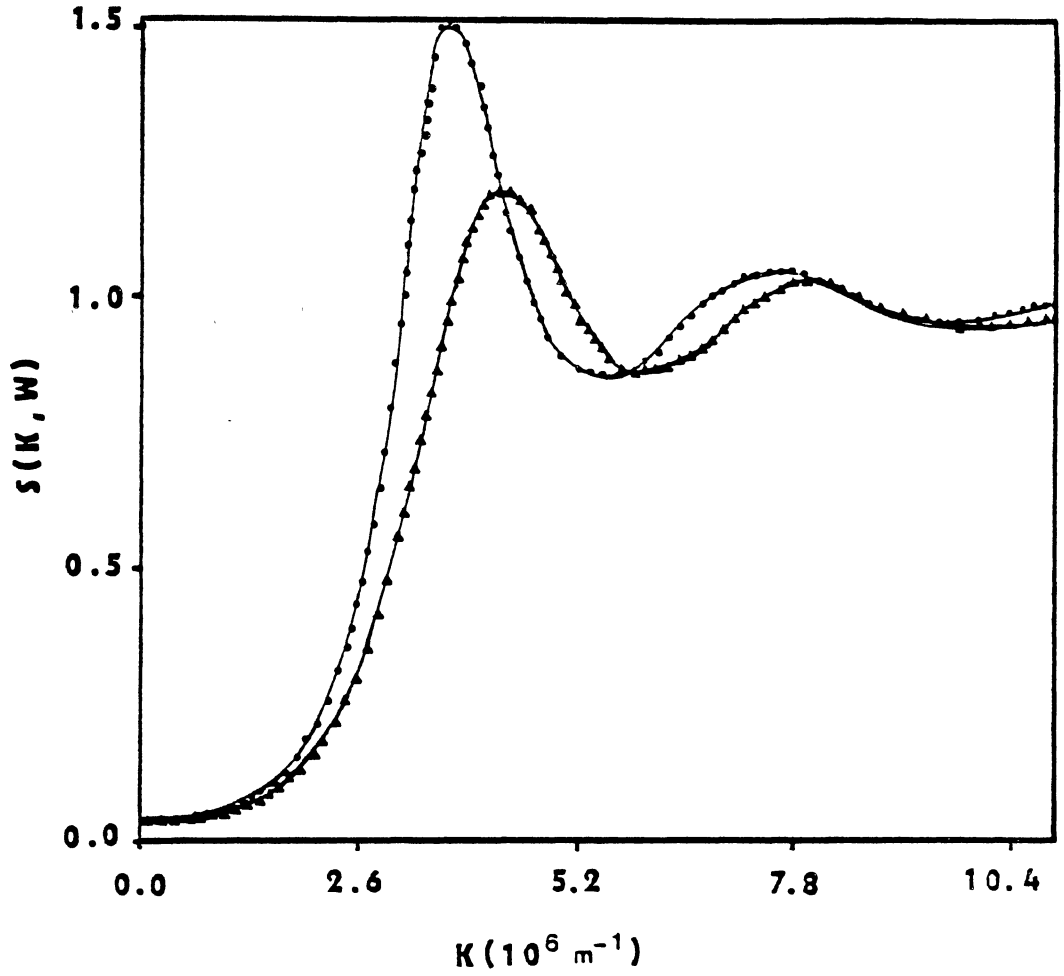

Figure 26. Calculated Structure Factor Using a Hyppernetted Chain Model
• • • Zero Shear Rate Reported in Reference (6)
▲ ▲ ▲ Nonequilibrium Values Calculated Along the Direction R1

Having gained some confidence in this theory and the validity of the computer program we proceeded to do some additional calculations concerning the distortion and decrease in the peak value of $S(\bar{k},w)$ along the directions $\hat{R}1$, $\hat{R}2$ and $\hat{R}3$ as a function of the rate of shear. These calculations were based on $S(k,0)$ for the linear chain model described earlier, since it is easily generated from equation (4-9).

As explained before, two different samples were used during this research. The scattering patterns indicate that sample A is a "fluid - solid" mixture having a stronger structure than the pure "fluid" sample B. This difference in the strength of the structure factor was simulated numerically by adjusting the value of $\alpha\beta$ in equation (4-9).

a. Numerical calculations involving sample A

To simulate the equilibrium structure factor of sample A, equation (4-9) was evaluated with $a = 8.1X10^{-7}m$ and $\alpha\ \beta = 4X10^{13}\ m^{-2}$; this produce an equilibrium structure factor $S(k,0)$ similar to that represented by the solid line in figure (25) but with a peak value of 5.3. This value is much larger than that expected by the Verlet criterion for freezing (peak value of 2.85) but produces agreement with observed distortion versus shear measurements. Using this equilibrium value, equation (4-10) was integrated numerically for different values of the shear rate w, to determine the distortion and decrease in the peak value

of $S(\bar{K},w)$. A value of Ds = 1 X $10^{-12} m^2/sec$ was used for the calculations.

Figure (27) shows the calculated distortion along the $\hat{R}1$ direction as a function of the shear rate. Note that this graph shows the same nonlinear behavior as that measured experimentally. This can be observed in figure (28) where we plot the calculated values (line with the circles) and the measured values (line with the squares).

Figure (29) shows the same calculated distortion this time plotted as a function of the square root of the rate of shear. This graph seems to indicate that the distortion calculated using equation (4-10) is directly proportional to the square root of the rate of shear and shows a similar behavior to the distortion measured experimentally and represented in figure (14) by the line with the circles.

b. Numerical calculations involving sample B

To simulate the equilibrium value S(k,0) of sample B, equation (4-9) was evaluated with a = $8.1X10^{-7}$ m and $\alpha\ \beta$ = 1.5 x 10^{13} m^{-2}; this produce an equilibrium structure factor S(k,0) similar to that represented by the solid line in figure (25) but with a peak value of 2.2 . Using this equilibrium value equation (4-10) was integrated numerically for different values of the shear rate w to determine the distortion and decrease in the peak value of $S(\bar{K},w)$. As before a value of Ds = 1 X 10^{-12} m^2/sec was used for the calculations.

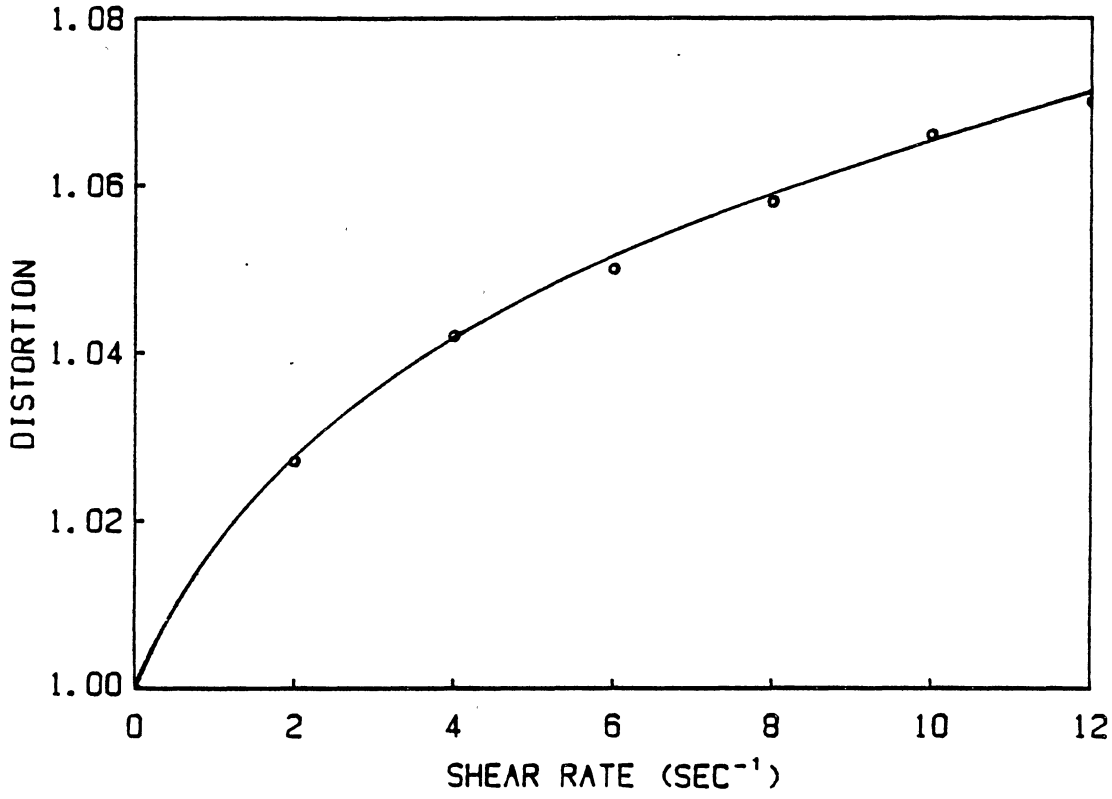

Figure 27. Calculated Distortion Along the Direction R1 as a Function of the Shear Rate. A Linear Chain Model of Strongly Interacting Particles was Used to Calculate the Equilibrium Values S(k,0); the Nonequilibrium Values S(k,w) were Calculated Using Equation (4-10)

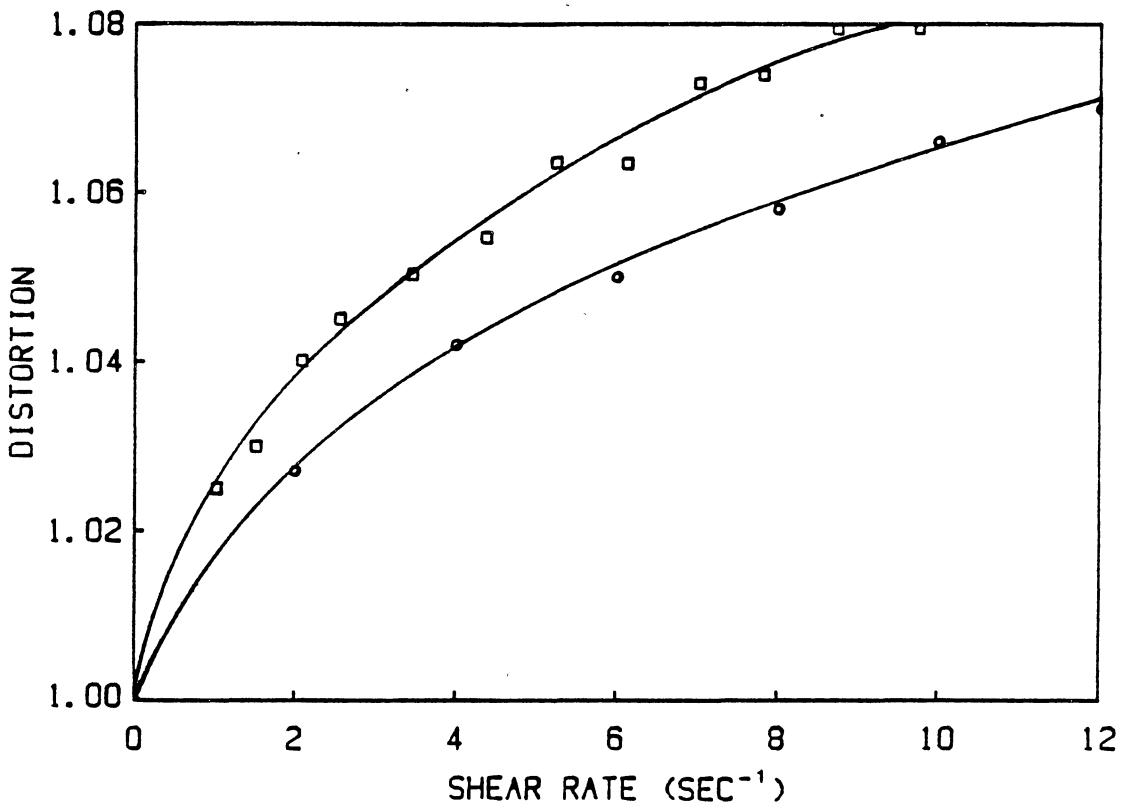

Figure 28. Distortion Along the Direction R1 as a Function of the Shear Rate.
□ □ □ Measured Values
o o o Calculated Values

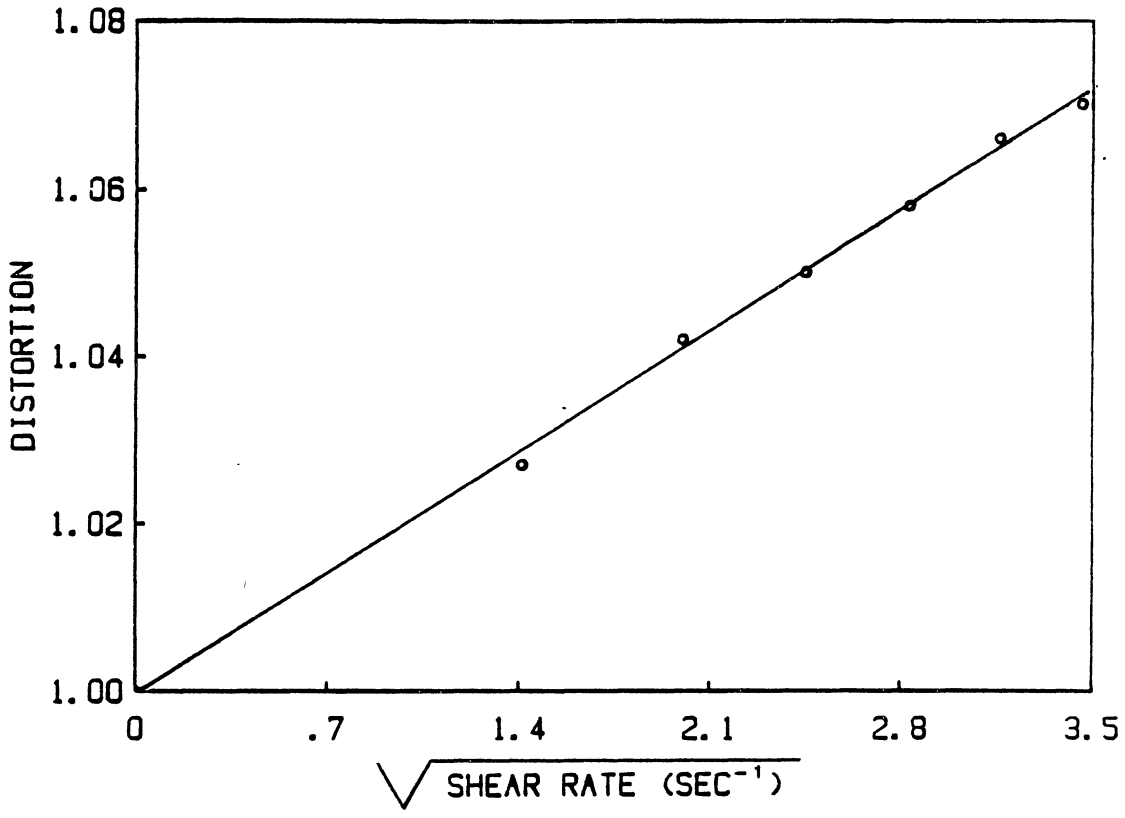

Figure 29. Calculated Distortion Along the Direction R1 as a Function of the Square Root of the Shear Rate. A Linear Chain Model of Strongly Interacting Particles was Used to Calculate the Equilibrium Values S(k,0); the Nonequilibrium Values S(k,w) were Calculated Using Equation (4-10).

Figure (30) and figure (31) show the calculated distortion along the direction $\hat{R}1$ as a function of the shear rate and the square root of the shear rate, respectively. Note the strong similarities between the calculated distortion shown in the last two graphs and the measured distortion represented by the line with the circles in figure (17) and figure (18).

If equation (4-10) is evaluated along the $\hat{R}3$ direction ($k_x = k_y = 0\ m^{-1}$) the result $S(\bar{k},w) = S(k,0)$ is obtained, indicating that this theory predicts no distortion and no intensity variation along the $\hat{R}3$ direction.

Having discussed the similarities between the calculated and measured distortion we now proceed to compare the calculated and measured peak values of $S(\bar{k},w)$ as a function of the shear rate. The equilibrium value $S(k,0)$ used to simulate sample A was used for these calculations. The calculated intensity variations along the direction $\hat{R}1$ as a function of the shear rate are shown in figure (32). The corresponding experimental data was presented in figure (23). Although the calculated values show a decrease in intensity greater than that observed experimentally the reader must keep in mind that the calculated values are strongly dependent on the equilibrium values used for the calculations. We have done some calculations using a weaker equilibrium value (peak value = 2.2) and the calculated decrease in intensity shows a more linear relationship with the shear rate than that shown in figure (32).

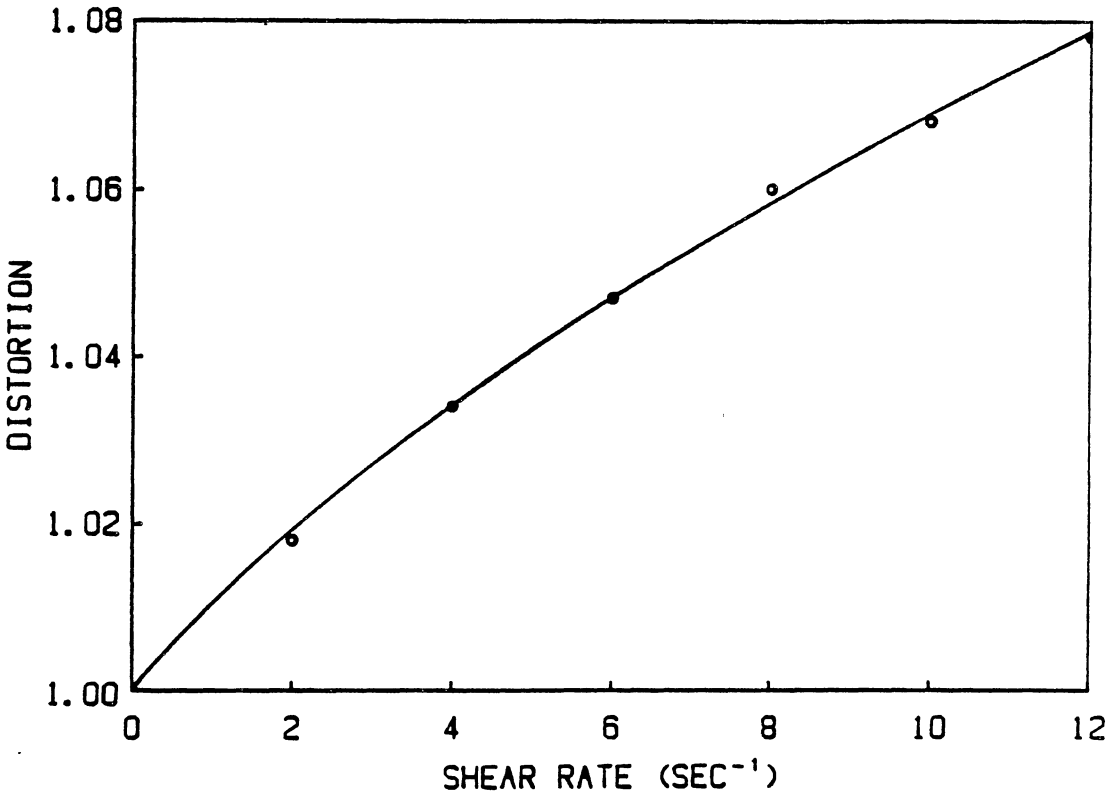

Figure 30. Calculated Distortion Along the Direction R1 as a Function of the Shear Rate. A Linear Chain Model of Weakly Interacting Particles was Used to Calculate the Equilibrium Values S(k,0); the Nonequilibrium Values S(k,w) were Calculated Using Equation (4-10)

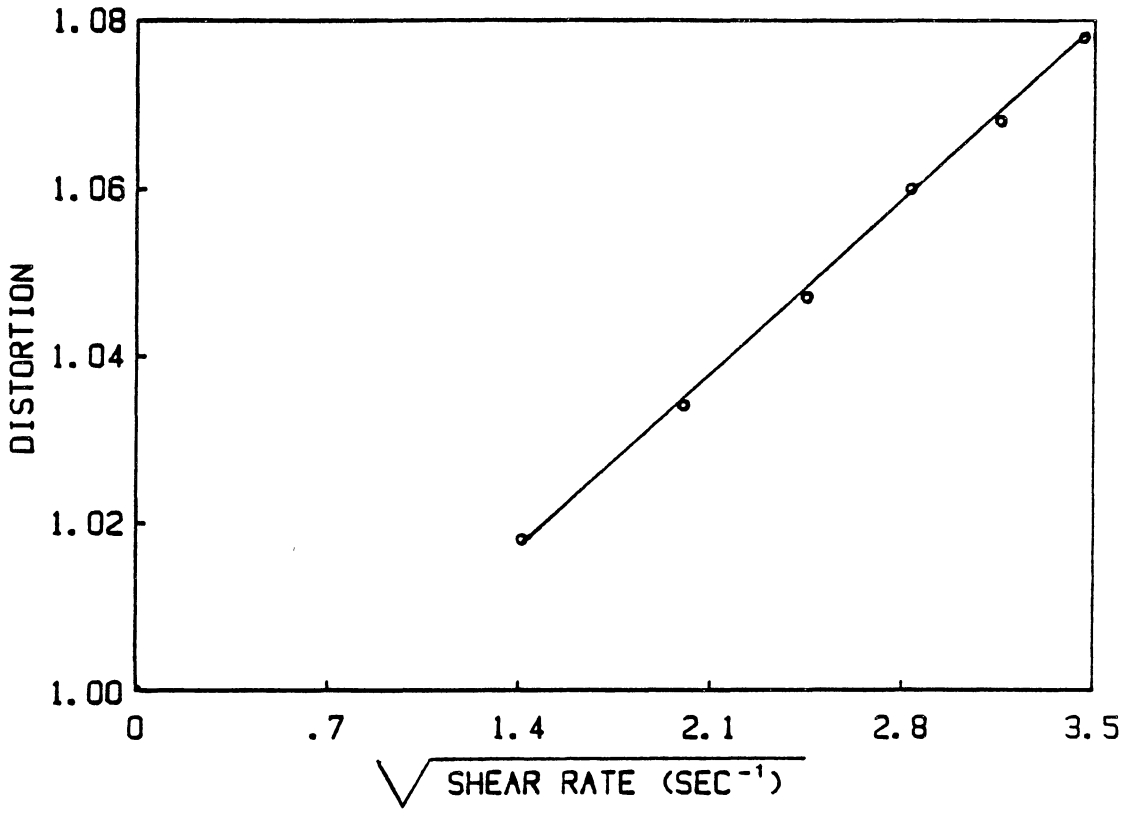

Figure 31. Calculated Distortion Along the Direction R1 as a Function of the Square Root of the Shear Rate. A Linear Chain Model of Weakly Interacting Particles was Used to Calculate the Equilibrium Values S(k,0); the Nonequilibrium Values S(k,w) were Calculated Using Equation (4-10)

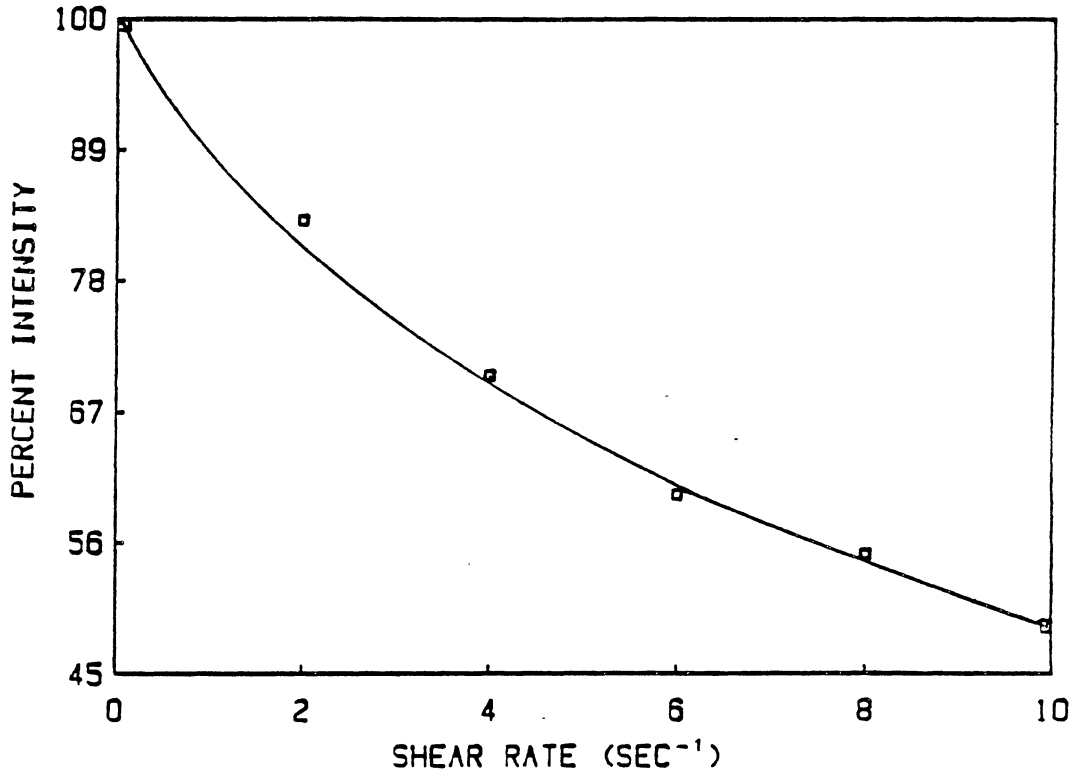

Figure 32. Calculated Changes in the Maximum of S(k,w) Along the Direction R1 as a Function of the Shear Rate. A Linear Chain Model of Strongly Interacting Particles was Used to Calculate the Equilibrium Values S(k,0); the Nonequilibrium Values were Calculated Using Equation (4-10)

CHAPTER V

SUMMARY AND SUGGESTIONS FOR FUTURE WORK

A. Summary of the Results

The scattering pattern of dilute colloidal systems undergoing shear flow has been investigated, two different samples were analyzed. All measurements were performed on the first peak of the structure factor (first Debye-Scherrer ring). We have found that the spherical scattering pattern at equilibrium degenerates into a distorted ellipsoid when the sample is sheared. A set of axes ($\hat{R}1$, $\hat{R}2$, $\hat{R}3$) can be defined based on the axes of the distorted ellipsoid. We have measured the shear induced distortion of the scattering pattern along the axes of the ellipsoid. Our experimental data show that this distortion is strongly dependent on the nature of the equilibrium value $S(k,0)$ and seems to be directly proportional to the square root of the applied shear rate. For the two samples analyzed the distortion along the major ($\hat{R}1$) and minor ($\hat{R}2$) axis of the ellipsoid is approximately 9% of the equilibrium value for a shear rate of 9 sec^{-1}. No appreciable distortion was detected along a direction perpendicular ($\hat{R}3$) to the plane containing the flow velocity and the velocity gradient. We have observed that the shear not only produces a distortion of the scattering

pattern, but also causes a decrease in the intensity of the Debye-Scherrer ring. Our measurements show that this intensity decrease also seems to depend of the nature of the equilibrium structure factor. A decrease of the intensity was observed along all three directions, $\hat{R}1$, $\hat{R}2$ and $\hat{R}3$, the intensity along the $\hat{R}3$ direction being the least affected.

Some measurements were performed to determine if the applied shear induces a change on the direction of maximum and minimum distortion; this effect will produce a rotation of the scattering pattern. Our measurements showed no appreciable rotation on the range of shear rate values 0 to 5 sec^{-1}; however, a shear rate of 40 sec^{-1} seems to produce a rotation of the scattering pattern.

Some theories have been developed to calculate the nonequilibrium structure factor of very dilute colloidal liquids of strongly interacting particles, in general these theories are based in a generalized form of the diffussion equation. We have analyzed three of these theories and we have found that the theory of Ronis (3, 6) have a good qualitative agreement with our measured data.

B. Suggestions for Future Work

Although we have analyzed two different samples and obtained some data to test the validity of the different theories, our comparison with the theory can be catalogued more qualitative than quantitative. The reason for this is that all the theories require a knowledge of the equilibrium

structure factor S(k,0) to calculate the nonequilibrium value $S(\bar{k},w)$. An accurate measurement of S(k,0) is difficult to obtain experimentally. Consequently, all calculated data and comparison with the theory is based on theoretical models. Ronis (6) has suggested that the hypernetted chain model (HNC) yields a much better fit to experimental data. Mainly all the calculations that we have reported are based on a linear chain of harmonically coupled particles (5). Consequently, one suggestion for future work is to evaluate $S(\bar{k},w)$ using the equilibrium values S(k,0) obtained from a HNC model. This could be an important point since our calculations show that the calculated data depends strongly on the equilibrium values S(k,0). For example, one may argue that the equilibrium values S(k,0) used to simulate sample A are not a realistic ones since a peak value of 5.3 is too large.

One point that needs further investigation is the decrease in the peak intensity of the first Debye-Scherrer ring along the $\hat{R}3$ direction (see figure (20)). As far as we know this intensity decrease cannot be explained with any of the theories discussed in this thesis. Another point that needs further investigation is that figure (24) shows that the direction of maximum distortion seems to be along the -50° rather than the -45° predicted by all the theories that we have discussed. This could be related to an experimental error or it could be a real effect.

As far as the experimental effort goes, one important problem to be solved is the noise in the intensity introduced by the digitizing process. Although we found that averaging several pictures improves greatly the quality of the data, this technique, as well as other image processing techniques, are difficult to implement in a small minicomputer like a LSI-11. However, we have recently acquired a more powerful computer that will allow us to process the images more efficiently allowing us to obtain more accurate data.

A SELECTED BIBLIOGRAPHY

1. B. J. Ackerson and N. A. Clark, Physical Review A 30, 906 (1984).

2. B. J. Ackerson and N. A. Clark, Physica A 118, 221 (1983).

3. D. Ronis, Physical Review Letters 52, 473 (1984).

4. J. C. Brown, P. N. Pusey, J. W. Goodwin and R. H. Ottewill, J. Phys A 8, 664 (1975).

5. B. J. Ackerson, The Journal of Chemical Physics 64, 242 (1976).

6. D. Ronis, Physical Review A 29, 1453 (1984).

7. R. L. Hoffman, Trans. Soc. Rheol. 16, 155 (1972).

8. T. A. Strivens, J. of Colloid and Interface Science 57, 476 (1976).

9. H. M. Laun, Makromolekulare Chemie (to be published).

10. M. Tomita and J. G. Van den Ven, J. of Colloid and Interface Science 99, 374 (1984).

11. P. Pieranski, Contemp. Phys. 24, 25 (1983).

12. J. C. Brown, P. N. Pusey, J. W. Goodwin and R. H. Ottewill, J. Phys A 8, 664 (1975).

13. W. J. Ashurst and W. G. Hoover, Physical Review A 11, 658 (1975).

14. D. J. Evans and H. J. M. Hanley, Physics Letters A 79, 178 (1980). Physics Letters A 80, 175 (1980).

15. D. Beysens and M. Gbadamassi, J. de Physique Lettres 21, L565 (1979).

16. S. Hess and H. J. M. Hanley, Physical Review A 25, 1801 (1982).

17. H. J. M. Hanley, J. C. Rainwater, N. A. Clark and B. J. Ackerson, J. Chem. Phys. 79, 4448 (1983).

18. W. J. Ashurst and W. G. Hoover, Physics Letters A 61, 175 (1977).

19. D. J. Evans, Physical Review A 23, 1988 (1981). Physical Review A 22, 290 (1980). Physica A 118, 51 (1983). Physics Letters A 74, 229 (1979).

20. B. C. EU, Physics Letters A 96, 29 (1983).

21. J. J. Erpenbeck, Physical Review Letters 52, 1333 (1984).

22. T. Yamada and K. Kawasaki, Prog. Theor. Phys. 53, 111 (1975). M. H. Ernst, B. Cichocki, J. R. Dorfman, J. Sharma, H. van Beijeren, J. Stat. Phys. 18, 237 (1978).

23. D. J. Evans, Physical Review A 25, 2788 (1982).

24. S. Hess, Physical Review A 22, 2844 (1980).

25. S. A. Rice and P. Gray, The Statistical Mechanics of Simple Fluids, John Wiley and Sons, New York (1965).

26. C. A. Croxton, Liquid State Physics - A Statistical Mechanical Introduction, Cambridge University Press, Great Brittain (1974).

27. G. H. A. Cole, An Introduction to the Statistical Theory of Classical Simple Dense Liquids, Pergamon Press, Oxford (1967).

28. I. Z. Fisher, Statistical Theory of Liquids, The University of Chicago Press, Chicago (1964).

29. G. Arfken, Mathematical Methods for Physicists, Academic Press, New York (1970).

APPENDIXES

APPENDIX A

A. MACROSCOPIC THEORY

1. The Continuity Equation

A fundamental law in Physics is the conservation of mass. In fluid mechanics this is expressed mathematically as the continuity equation.

$$\frac{\partial \rho}{\partial t} = -\bar{\nabla}\cdot(\rho\ \bar{V}) \qquad \text{(A-1)}$$

Where ρ and $\bar{V}$ are the density and the velocity of the fluid, respectively. Note that for an incompressible fluid, the continuity equation simplifies to:

$$\bar{\nabla}.\bar{V} = 0 \qquad \text{(A-2)}$$

2. The Stress Tensor

For the stress-strain relationship of a simple fluid we introduce the Newtonian law:

$$\overleftrightarrow{\sigma} = -p\overleftrightarrow{1} + 2\eta\overleftrightarrow{\varepsilon} \qquad \text{(A-3)}$$

where $\overleftrightarrow{\sigma}$ and $\overleftrightarrow{1}$ are the stress tensor and the unit tensor, respectively. The equilibrium pressure is given by p and the coefficient of shear viscosity by η . The rate of strain tensor $\overleftrightarrow{\varepsilon}$ is defined as:

$$\overleftrightarrow{\varepsilon} = \tfrac{1}{2} \left(\bar{\nabla}\bar{V} + \widetilde{\bar{\nabla}\bar{V}}\right) \qquad \text{(A-4)}$$

where

$$(\widetilde{\bar{\nabla}\bar{V}})_{ij} = (\bar{\nabla}\bar{V})_{ji}$$

In writing equation (A-3) we have assumed that the liquid is incompressible (i.e., $\bar{\nabla}.\bar{V} = 0$).

B. MICROSCOPIC THEORY

1. The Stress Tensor

From a microscopic point of view the stress tensor is written as:

$$\overleftrightarrow{\sigma} = \overleftrightarrow{\sigma}_k + \overleftrightarrow{\sigma}_\Phi \qquad \text{(A-5)}$$

The term $\overleftrightarrow{\sigma}_k$ corresponds to the transport of momentum by molecular translation, the term $\overleftrightarrow{\sigma}_\Phi$ corresponds to the interaction contribution to momentum transport. Consequently, $\overleftrightarrow{\sigma}_k$ is called the kinetic part and it is the dominant part in dilute gases; $\overleftrightarrow{\sigma}_\Phi$ is called the potential part and it is the dominant part for dense gases and fluids.

We are concerned here with the potential part $\overleftrightarrow{\sigma}_\Phi$. It can be shown (25) that $\overleftrightarrow{\sigma}_\Phi$ is related to the radial distribution function $g(\bar{r})$ by the following relation:

$$\overleftrightarrow{\sigma}_\Phi = (n^2/2) \int \frac{\bar{r}\bar{r}}{r} \Phi'(r)\, g(\bar{r})\, d\bar{r} \qquad \text{(A-6)}$$

where n is the particle density and $\Phi(r)$ is the intermolecular potential. The distribution function $g(\bar{r})$ plays an exceptionally important role in the theory of

liquids, in fact the molecular structure of simple liquids is in many respects determined by the function $g(\bar{r})$.

APPENDIX B

A FORTRAN PROGRAM TO EVALUATE EQUATION (4-10) NUMERICALLY

```
C RONIS INTEGRAL EVALUATED ALONG LINE
C OF MAXIMUM DISTORTION
C SK0 CONSISTS OF 1150 DATA POINTS STORED IN FILE SK0
C IFKY1 IS THE STARTING POINT IN REAL SPACE (1 TO 1150)
C IFKY2 IS THE FINAL POINT IN REAL SPACE (1 TO 1150)
C TO OBTAIN DISTANCE IN K-SPACE USE K=DISTANCE*1E4
C AUGUST 29,1985     NEMESIO CARABALLO
      DIMENSION SK0(1600),TI(1600)
      DS=1.E-12
      CKT=1.E4
      FKTMAX=2.E8
C READ EQUILIBRIUM VALUE S(K,0)
      OPEN(1,FILE='SK0',STATUS='OLD',FORM='UNFORMATTED')
      READ(1)(SK0(J),J=1,1150)
      CLOSE(1)
 300  WRITE(*,*)'ENTER SHEAR'
      READ(*,*)IW0
      W0=FLOAT(IW0)
      WRITE(*,*)'ENTER IFKY1'
      READ(*,*) IFKY1
      WRITE(*,*) 'ENTER IFKY2'
      READ(*,*) IFKY2
      WRITE(*,200)
 200  FORMAT(////////////////////////////)
      WRITE(*,50)
      DO 10 IFKY=IFKY1,IFKY2
      FKY=CKT*FLOAT(IFKY)
      FNMAX=(FKTMAX+ABS(FKY))/CKT
      C=2.*DS/ABS(W0*FKY)
      ATI=0.
      IFNMAX=INT(FNMAX)
      DO 20 IFM=0,IFNMAX
      FM=FLOAT(IFM)
      ARG=-(FKY)+FM*CKT
      IARG=INT(ABS(ARG/CKT))
      IF(IARG.GT.1150) ZAVG=1.
      IF(IARG.GT.1150) GO TO 100
      ZAVG=(SK0(IARG)+SK0(IARG+1))/2.
 100  ATI=ATI+C*CKT*(ARG**2+FKY**2)/ZAVG
      IF(INT(ATI).GT.86) ISTOP=IFM
```

```
      IF(INT(ATI).GT.86) GO TO 26
      TI(IFM+1)=ATI
20    CONTINUE
26    SK=0.
      TI(ISTOP-1)=88.
      TI(ISTOP)=88.
      TI(ISTOP+1)=88.
      DO 30 N=0,ISTOP
      FN=FLOAT(N)
      BRG=-(FKY)+FN*CKT
      EXPO=EXP(-TI(N+1))
      SK=SK+C*CKT*(BRG**2+FKY**2)*EXPO
30    CONTINUE
      WRITE(*,31) IW0,IFKY,SK0(IFKY),SK
10    CONTINUE
      GO TO 300
31    FORMAT(1X,I3,8X,I6,10X,F9.6,10X,F9.6)
50    FORMAT(1X,'SHEAR',8X,'DISTANCE',10X,'SK0',14X,'SK')
      END
```

VITA

Nemesio Caraballo

Candidate for the Degree of

Doctor of Philosophy

Thesis: LASER LIGHT SCATTERING STUDY OF LOCAL ORDER IN SHEARED COLLOIDAL LIQUIDS

Major Field: Physics

Biographical:

Personal Data: Born in Ponce, Puerto Rico, September 28, 1950, the son of Mrs. Leonor Ramos-Lopez and the late Nemesio Caraballo-Perez.

Education: Graduated from Washington Irving High School, Adjuntas, Puerto Rico, in May, 1967; received Bachelor of Science Degree in Education from Catholic University of Puerto Rico in December, 1971; received Master of Science Degree from University of Arkansas in May, 1981; completed requirements for the Doctor of Philosophy Degree at Oklahoma State University in December, 1985.

Professional Experience: High School Physics Teacher, Department of Education of Puerto Rico, January, 1972 to December, 1978; Instructor of Computer Sciences, Department of Business Administration, Catholic University of Puerto Rico, September, 1977 to December, 1978; Research Assistant, Department of Electronic and Instrumentation, University of Arkansas, January, 1979 to December, 1980; Teaching Assistant,Department of Physics, Oklahoma State University, January, 1981 to May, 1985; Research Assistant, Department of Physics, Oklahoma State University, January, 1983 to August, 1985.